

Review

Effect of Material Selection and Surface Texture on Tribological Properties of Key Friction Pairs in Water Hydraulic Axial Piston Pumps: A Review

Yingna Liang ^{1,2,*} , Wei Wang ^{1,2}, Zhepeng Zhang ^{1,2}, Hao Xing ^{1,2}, Cunyuan Wang ^{1,2}, Zongyi Zhang ^{1,2}, Tianyuan Guan ^{1,2} and Dianrong Gao ^{1,2,*}

¹ School of Mechanical Engineering, Yanshan University, Qinhuangdao 066004, China

² Hebei Provincial Key Laboratory of Heavy Machinery Fluid Power Transmission and Control, Yanshan University, Qinhuangdao 066004, China

* Correspondence: liangyingna@ysu.edu.cn (Y.L.); gaodr@ysu.edu.cn (D.G.)

Abstract: A water hydraulic axial piston pump has become the preferred power component of environmentally friendly water hydraulic transmission systems, due to its advantages of a compact structure, high power density, and so on. The poor friction and wear performance in the water medium, especially under extreme conditions of high speed and high pressure, limit the engineering application of the water hydraulic axial piston pump. In this review, the research progress for key friction pair materials (such as special corrosion-resistant alloys, engineering plastics, and engineering ceramics) for water hydraulic axial piston pumps is, firstly, summarized. Secondly, inspired by nature, the processing methods, lubrication drag-reduction mechanism, and tribological properties of the biomimetic surface textures are discussed. The effects of the surface texture shape, equivalent diameter, depth, and arrangement on the pump's tribological properties are reviewed in detail. Finally, the application status of, and problems with, surface texture technology in water hydraulic axial piston pumps are summarized. It is suggested that future studies should focus on the multi-field coupling lubrication anti-friction mechanism of the multi-type composite texture under extreme conditions and mixed lubrication; and the anti-wear performance of the texture coupled with a coating modification, to further promote the surface texture in the field of lubrication antifriction engineering applications.

Keywords: water hydraulic axial piston pump; friction pair material; biomimetic surface texture; friction; wear; lubrication



Citation: Liang, Y.; Wang, W.; Zhang, Z.; Xing, H.; Wang, C.; Zhang, Z.; Guan, T.; Gao, D. Effect of Material Selection and Surface Texture on Tribological Properties of Key Friction Pairs in Water Hydraulic Axial Piston Pumps: A Review. *Lubricants* **2023**, *11*, 324. <https://doi.org/10.3390/lubricants11080324>

Received: 13 June 2023

Revised: 19 July 2023

Accepted: 28 July 2023

Published: 31 July 2023



Copyright: © 2023 by the authors. Licensee MDPI, Basel, Switzerland. This article is an open access article distributed under the terms and conditions of the Creative Commons Attribution (CC BY) license (<https://creativecommons.org/licenses/by/4.0/>).

1. Introduction

1.1. Development of Hydraulic Transmission Technology

Water hydraulic technology is a green transmission technology that uses filtered fresh water or seawater, instead of mineral oil, as the working medium. As early as 1795, the British inventor Joseph Braman. invented the world's first water hydraulic press and, in the following 100 years, hydraulic systems were based on water as the working medium [1].

At the beginning of the 20th century, with the rise of the petroleum industry and the development of oil-resistant sealing materials, such as butadiene rubber, the mineral oil hydraulic medium, with its good comprehensive physical and chemical properties, soon replaced water, and became the most important working medium in hydraulic systems [2]. In 1905, American professor Harvey W., and engineer Reynold J. developed an oil hydraulic axial piston pump. However, mineral oil has two serious shortcomings, inflammability and pollution, which not only make oil hydraulic transmission difficult to popularize and apply in the food, beverage, medicine, electronics, packaging, and other industries, but have also caused it to gradually lose its applications in metallurgy, hot rolling, casting, and

other high-temperature, open-flame occasions, and in coal-mine, underground, and other flammable, explosive environments [1,3,4].

As ecological environmental protection, safe production, and energy conservation receive more and more attention, the outstanding advantages of the water medium, such as no pollution, a low cost, safety, and good dynamic characteristics mean that water hydraulic technology has incomparable advantages in some applications, and has attracted the general attention of the international hydraulic field and engineering circles, once again [5–10]. Meanwhile, the physical and chemical characteristics of the water medium, such as a low viscosity, poor lubrication, strong corrosion, and high vaporization pressure also bring about a series of inevitable common technical problems in the development of water hydraulic components and systems, such as lubrication and sealing, friction and wear, corrosion, and cavitation [11–13]. In recent years, the rapid development of engineering ceramics, polymer materials, and other new engineering materials [14,15], the progress of precision machining technology, and the appearance of bionic tribology [16–18] suggest that the key technical problems faced by the research into water hydraulic technology can be effectively solved, to promote the rapid development of water hydraulic technology.

1.2. Water Hydraulic Axial Piston Pumps

The research and development of water hydraulic components is the fundamental power in promoting the development of water hydraulic technology. The water hydraulic pump is the key power component of the water hydraulic system, which converts the mechanical energy (torque T , speed n) output of the prime mover (motor, internal combustion engine, etc.) into the hydraulic energy of the transmission medium, transports the hydraulic energy in the form of pressure p and flow q to the hydraulic system, and drives the hydraulic actuator to work externally. The efficiency of the water hydraulic pump determines the quality efficiency and service life of the water hydraulic system [4].

The structure and working principle of an axial piston pump, used in several types of mainstream hydraulic pumps, are shown in Figure 1. The pump consists of a swash plate (2), slippers (3), pistons (4), a cylinder block (5), a port plate (7), and other main parts. The swash plate (2) and port plate (7) are fixed, the drive shaft (14) drives the cylinder block (5) and the pistons (4) to rotate together, and the slippers (3) are pressed against the swash plate (2) by the return plate (12). When the drive shaft rotates in the direction shown in the figure, the piston gradually extends out of the cylinder block in the half circle rotating along the swash plate from outside to inside, so that the volume of the sealing working chamber in the cylinder hole continues to increase, resulting in a local vacuum, which inhales the liquid through the suction window of the port plate. The piston is gradually pushed into the cylinder in the half circle rotating from inside to outside, so that the volume of the sealing working chamber in the cylinder hole is continuously reduced, and the liquid is discharged from the drain window of the port plate to the system.

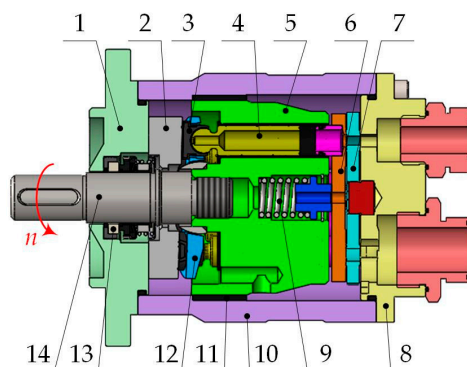


Figure 1. Structure of the water hydraulic axial piston pump: 1—pump front cover, 2—swash plate, 3—slider, 4—piston, 5—cylinder block, 6—thrust plate, 7—port plate, 8—pump rear cover, 9—spring, 10—pump shell, 11—sliding bearing, 12—return plate, 13—shaft seal, 14—drive shaft.

The piston pump depends on the reciprocating movement of the pistons in the cylinder hole to achieve the functions of liquid suction and liquid ejection. From a manufacturing process, it is easier to obtain a small clearance fit between the cylindrical piston and the cylinder hole. From a design perspective, it is easier to ensure that the piston has a sufficient sealing length inside the cylinder hole [19,20]. The Naval Civil Engineering Lab (NCEL) of the United States carried out an in-depth calculation and analysis of the force condition of the gear pump, vane pump, and axial piston pump, and found that the pv value in the friction pair of the axial piston pump is much smaller than those of the other two pumps, which is more conducive to reducing the requirements of wear resistance in the materials [21]. Therefore, the water hydraulic axial piston pump can be used as the preferred power element in the water hydraulic system.

However, there are still some technical problems to solve. The corrosion of water is strong, which means that the parts made of metal materials in oil axial piston pumps corrode and rust easily in the water medium, especially the key friction pairs, such as the slipper pair, piston pair, and barrel/port plate pair [11]. Due to the low viscosity and poor lubrication of water, if the clearance of the friction pair is too large, it will lead to leakage. If the clearance of the friction pair is too small, the lubricating water film cannot be formed, resulting in the direct contact of the friction pair surfaces, and increased friction, wear, and overturning in the slipper [4,12].

Based on the friction and wear characteristics, and lubrication mechanism of the key friction pair of water hydraulic axial piston pumps, this paper systematically discusses the effects of material selection and surface texture on the corrosion resistance and tribological properties of friction pairs under water-lubricated conditions, hoping to provide a valuable reference for the design, development, and application of water hydraulic axial piston pumps, and other water hydraulic components.

2. Materials

Selecting a suitable material pairing is the primary method of improving the friction performance of key friction pairs in water hydraulic axial piston pumps. Scholars have conducted much research on the search for friction-pair materials with corrosion resistance, wear resistance, and self-lubricating properties. It has been found that special corrosion-resistant alloys [22,23], engineering plastics [24], and engineering ceramics [25] are materials suitable for key friction pairs, and have been verified via engineering practice.

2.1. Special Corrosion-Resistant Alloy

Some special metal alloys (stainless steel, titanium alloy, nickel alloy, aluminum alloy, etc.) are very suitable for use in water lubrication, especially in seawater lubrication environments, because of their excellent high specific strength, corrosion resistance, and high–low temperature resistance. Seawater has the interaction of lubrication, cooling, and corrosion on the friction pair [26–28]. Lubrication and cooling make the friction coefficient under seawater conditions lower than that under pure water and dry friction conditions, while corrosion accelerates the abrasion of alloys. The alloy friction pairs of Cu-6Sn-6Zn-3Pb/AISI321 stainless steel [26], ZChSnSb8-8 alloy/52100 stainless steel [27], TC4 alloy/316 stainless steel, Hastelloy C-276 alloy/316 stainless steel, Inconel 625 alloy/316 stainless steel, and Monel K500 alloy/316 stainless steel [28] are all dominated by abrasive wear and plastic deformation under pure water and dry friction conditions, while the friction behaviors become abrasive wear, plastic deformation, and corrosion wear under seawater conditions. Zhang's research [29] showed that 304 austenitic stainless steel (with a low fault energy) is prone to martensitic phase transition under the action of friction stress in a seawater environment. The martensitic phase with high hardness improves the wear resistance of stainless steel, but the phase transition intensifies the electric coupling corrosion on the friction contact surface, thus causing the synergistic effect of corrosion and wear, as shown in Figure 2 [29].

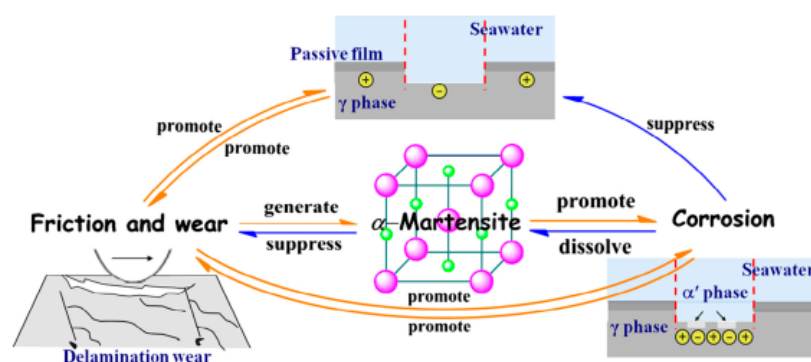


Figure 2. Schematic showing the effect of α' -martensite on tribocorrosion during sliding [29].

The surface of a titanium alloy will immediately form a protective film in constant-temperature seawater, so that it is in a passivated state [30], and no pitting or crevice corrosion occurs. Ding et al. [31] found that the friction coefficient of the TC11/GCr15 pair in artificial seawater is lower than that in pure water. The reason is that, with the increase in the load, the local stress of the friction contact point increases, and fine grinding chips are formed under the action of normal stress. These chips act like “ball bearings” in seawater, to further reduce the friction coefficient [32]. The lubrication film formed on TC11 in seawater also helps to reduce the friction coefficient, but its wear is higher than that in pure water, because corrosion by the seawater accelerates the wear. The wear mechanism of TC11 in seawater is mainly fatigue shedding and abrasive wear. Li et al. [33] studied the tribological behavior of TC4/GCr15 friction pairs in the environments of air, pure water, and simulated seawater, and also reached a similar conclusion.

Table 1 shows the comparison of corrosion, wear, and interaction in different metallic materials. Austenitic stainless steel (316L) can improve chloride ion corrosion resistance, and is more suitable for moving parts in corrosive seawater environments than martensitic stainless steel (304). Compared with single austenitic stainless steel, ferrite and austenitic duplex steel (2205) can further improve the corrosion resistance of parts, and prolong the service life in corrosive media. Titanium alloy (Ti6Al4V) has better wear and corrosion resistance. However, the corrosion-accelerated wear of titanium alloy is about 37% of the total material loss, indicating that corrosion is the key factor leading to the total wear damage of titanium alloy. The pure mechanical wear rate of aluminum alloy (2024) is approximately 98.1–80.2%, which is significantly higher than that of stainless steel and titanium alloy, and becomes the key factor leading to abrasion failure in aluminum alloy. Therefore, improving the wear resistance of the aluminum alloy is the primary problem faced when applying it to moving parts in a corrosive medium. Compared to stainless steel and titanium, nickel alloy (Monel K500) performs well in terms of both mechanical properties and corrosion resistance, making it more suitable for moving parts in harsh corrosive environments.

2.2. Engineering Plastics

Compared with metal, engineering plastics (polymer composites) can undergo deformation under certain conditions, and have a better complete recovery ability. The property of embedding abrasive particles greatly improves the wear resistance, meaning that engineering plastics can be widely used as a key material for friction pairs in the water environment. It has been found that polytetrafluoroethylene (PTFE), polyether ether ketone (PEEK), polyimide (PI), polyamide (PA), polyphenylene sulfide (PPS), and ultra-high molecular weight polyethylene (UHMWPE) are several types of polymer composite material with potential lubrication in the water environment. The tribological properties, and friction and wear mechanisms are shown in Table 2.

Table 1. Comparison of corrosion, wear, and interaction in different metallic materials [34–39].

Materials	Conditions				Friction Coefficient	Material Loss Rate/(mm ³ ·mm ⁻² ·y ⁻¹)				
	Medium	Speed	Load	Potential		Total	Pure Mechanical Wear	Corrosion without Wear	Wear Accelerated Corrosion	Corrosion Accelerated Wear
304/Al ₂ O ₃	Seawater	80 r/min	80 N	−0.7 V	0.375	360	360	—	—	—
				OCP ¹	0.405	530	359.96	0.04	10	160
				+0.1 V	0.427	650	359.9	0.1	17	273
410/Al ₂ O ₃	Seawater	80 r/min	80 N	−0.7 V	0.397	520	520	—	—	—
				OCP ¹	0.435	730	514.87	0.13	22	193
				+0.1 V	0.380	610	529.6	0.4	55	25
2205/Al ₂ O ₃	Seawater	20 mm/s	100 N	−0.8 V	0.420	127.80	127.80	—	—	—
				OCP ¹	0.425	103.38	90.34	0.000437	0.22	12.82
316L/Al ₂ O ₃	Pure water	200 r/min	100 N	OCP ¹	0.55	145.0	—	—	—	—
	Seawater			0.43	185.4	134.8	0.0308	1.7	48.2	
OCP 1	Pure water	200 r/min	100 N	OCP ¹	0.29	42.0	—	—	—	—
	Seawater			0.24	68.7	43.8	0.00493	2.2	22.7	
OCP 1	Seawater	200 r/min	100 N	−0.6 V	0.22	1.56	1.56	—	—	—
				OCP ¹	0.17	2.18	1.56	0.00245	0.25	0.37
				+0.1 V	0.12	3.42	1.56	0.00791	0.65	1.2
				+0.5 V	0.09	5.93	1.56	0.01697	2.05	2.3
2024 Aluminum alloy/Al ₂ O ₃	Seawater	20 mm/s	5 N		0.490	1012.0	993.9	0.00152	0.2	17.9
			25 N	OCP ¹	0.465	4111.2	3682.0	0.00152	1.7	427.5
			50 N		0.455	7472.4	5995.1	0.00152	1.9	1475.4

¹ Open circuit potential (OCP).

Table 2. Tribological properties, and friction and wear mechanism of several engineering plastics in the water environment.

Materials	Tribological Properties	Friction and Wear Mechanism	References
PTFE	Excellent self-lubrication, chemical corrosion resistance, and high- and low-temperature resistance Low water absorption and hydrophobicity	It is difficult to form a transfer film on the counter surface. The friction and wear properties are improved by water boundary lubrication and cooling.	[40]
PEEK	Good mechanical properties and chemical stability Many hydrophilic carbonyl groups in the macromolecular chains	(1) The hydrophilic carbonyl groups form a strong adsorption film with the water molecules, forming a boundary lubrication film between the friction interfaces. (2) Water molecules penetrate the surface of PEEK, causing swelling, the surface shear strength decreases, and the friction coefficient decreases. (3) The strong heat dissipation of water rapidly dissipates frictional heat, and the frictional surface is in a viscoelastic or even glass state, which significantly reduces the adhesive transfer of PEEK to the frictional counter surface.	[41]
PI	Excellent specific strength, high- and low-temperature resistance, radiation resistance, and chemical corrosion resistance	(1) The polar amide groups contained in PI easily combine with water molecules through hydrogen bonding, forming a water adsorption film on the friction surface to lubricate. (2) The surface absorbs water, causing the swelling, shear strength, friction coefficient, and wear rate to decrease.	[42]
PA	Stable chemical properties, high mechanical strength, and low friction coefficient with steel	(1) PA does not easily form transfer film on the counter surface because of its high water absorption, and mechanical micro-cutting continues to occur. (2) Friction heat intensifies the hydrolysis of amide groups in the molecules and the action of water molecules, weakens the hydrogen bond between the surface molecules, partially breaks the C-C bond, softening and damaging the material surface, and leads to a higher wear loss than dry friction.	[43,44]
PPS	Excellent high-temperature resistance, corrosion resistance, anti-friction and wear resistance, dimensional stability, mechanical properties, thermal conductivity, and cohesiveness	(1) PPS friction coefficient decreases. (2) Water can penetrate the material surface, resulting in reduced strength and increased wear.	[45]
UHMWPE	An engineering plastic of linear structure, with excellent impact resistance, self-lubrication, corrosion resistance, and low water absorption.	The hardness of the matrix is low, and the resistance to abrasive wear is poor.	[46]

As shown in Table 2, engineering plastics generally have excellent self-lubrication and corrosion resistance in water environments, but they have a low mechanical strength and poor wear resistance. Their comprehensive performance can be improved by filling and blending. The common filling methods are fiber filling, particle filling, and mixed filling.

Carbon fiber (CF) and glass fiber (GF) are the main fibers used in the reinforced modification of engineering plastics. CF has a high strength, good thermal conductivity, and corrosion resistance, and can be firmly combined with the matrix to improve the strength and hardness of polymer composites. In the friction process, most of the load is borne by the CF, with good wear resistance, which prevents the micro-peaks on the counterparts from plowing the matrix [47,48]. In addition, the cooling effect of water helps to maintain the material strength, and inhibit fiber shedding, reducing the wear to the matrix material. However, the scraping action of CFs will affect the formation of the transfer film on the counter surface [49]. GF has the advantages of strong heat resistance, good corrosion resistance, and a high tensile strength, but it is brittle and easy to break. Yang [50] found that GFs can prevent crack propagation, and reduce the wear of PTFE. However,

when the content of the GFs increases to 30%wt, a large number of prominent GFs will scrape the counter surface, and prevent the formation of the transfer film. In addition, GF is weakly bound to the matrix, and is easily peeled off under friction force, increasing the friction and wear. PTFE, graphite, MoS₂, and ceramic powder are the main particle fillers used in the modification of engineering plastics [51]. Via the mixing of the fiber and particle filling, the two can promote each other, and synergistically improve the performance of the composite materials [52].

2.3. Engineering Ceramics

Compared with metal, the elastic modulus of engineering ceramic is about 50% higher than that of steel, the compressive strength is about 5–7 times that of steel, the mass is about 40% that of steel of the same volume, the thermal expansion coefficient is about 20% that of steel, and the hardness can reach 1700 [53]. However, engineering ceramic has a greater brittleness, and a poor embedding performance, so it easily causes more serious abrasive wear than metal.

As shown in Table 3, researchers studied the friction and lubrication mechanism of Si₃N₄/Si₃N₄, SiC/SiC, Al₂O₃/Al₂O₃, Ti₃AlC₂/Si₃N₄, Ti₃AlC₂/SiC, Ti₃AlC₂/Al₂O₃, and so on, in a water/seawater environment, and proposed the Tribochemical Wear Theory. It is found that the lubrication film is formed on the friction surface of ceramic materials through a tribochemical reaction in a water-lubricated environment, which reduces the friction coefficient and wear rate. The interaction of Na⁺ with other ions in seawater can accelerate the formation of the lubrication film, meaning that it has better tribological characteristics. Ceramic friction pairs are mainly influenced by the interaction between mechanical wear and friction chemical wear, and the boundary lubrication gradually transforms into hydrodynamic lubrication or mixed lubrication in the friction process.

Table 3. Tribological properties of several ceramic materials in a water/seawater environment.

Friction Pair	Friction Coefficient	Friction and Lubrication Mechanism	Tribochemical Reaction Film	References
Si ₃ N ₄ /Si ₃ N ₄	0.002 (under water)	hydrodynamic lubrication, mixed lubrication	Si(OH) ₄	[54,55]
SiC/SiC	0.013 (under seawater)	tribochemical wear	SiO ₂	[56,57]
Al ₂ O ₃ /Al ₂ O ₃	0.2 (under water)	mechanical wear	--	
Al ₂ O ₃ /Al ₂ O ₃	0.12 (under seawater)	boundary lubrication	Al(OH) ₃	[58]
Ti ₃ AlC ₂ /Si ₃ N ₄	0.54 (under seawater)	tribochemical wear	--	
Ti ₃ AlC ₂ /SiC	0.14 (under seawater)	mechanical wear	--	
Ti ₃ AlC ₂ /SiC	0.14 (under seawater)	boundary lubrication	TiO ₂ , Al ₂ O ₃ and SiO _x	[59,60]
Ti ₃ AlC ₂ /Al ₂ O ₃	0.5 (under seawater)	tribochemical wear	--	
Ti ₃ AlC ₂ /Al ₂ O ₃	0.5 (under seawater)	mechanical wear	--	

The rapid development of special corrosion-resistant alloys, engineering plastics, and engineering ceramics provides an important basis for the selection of key friction pair materials in water hydraulic axial piston pumps and also lays an important technical foundation for the revival of water hydraulic technology. In addition, on the premise of not damaging the properties of materials, surface engineering technologies, such as ion implantation and surface coating, are used to strengthen or regenerate the surface properties of materials, so that the surface of a material has excellent tribological properties [61,62]. In recent years, this has become an important method of realizing the properties of water hydraulic equipment materials.

3. Biomimetic Surface Texture

Over the long history of hundreds of millions of years, plants and animals have constantly evolved to adapt to their living environment. Most of the surface of organisms in nature presents a variety of microscopic non-smooth structures, which allow them excellent

desorption, drag reduction, and wear resistance functions. In 1960, Steele J first proposed the concept of “bionics” at the first Bionics Forum in the United States. Bionic tribology is an important branch of bionics [63], and provides a new approach to solving the corrosion and wear problem of the key friction pairs in water hydraulic axial piston pumps.

Through the study of applying the biomimetic surface texture in the friction pairs under different working conditions, it is found that the tribological properties are improved by the proper texture shape, equivalent diameter, depth, and arrangement of the biomimetic surface texture. Advanced processing methods provide important technical support in the realization of the biomimetic surface texture. The detailed classification of current mainstream processing methods is shown in Figure 3 [64].

3.1. Mechanisms

Hamilton [65] first proposed the lubrication theory of micro-irregularities in 1966, which is the initial expression of surface texture. Etsion [66–68] established the lubrication model of the textured mechanical seal under hydrodynamic pressure, and analyzed the antifriction effect of the textured surface, theoretically and experimentally. Since then, the effectiveness of the surface texture in improving tribological properties has been widely discussed.

The lubrication antifriction mechanism of the surface texture is related to the lubrication state, which mainly includes fluid lubrication, boundary lubrication, and dry friction. The Stribeck curve (Figure 4) [69] can present the three different types of lubrication states: boundary lubrication ($\lambda < 1$, λ is the ratio of surface separation and comprehensive roughness), mixed lubrication ($1 < \lambda < 3$), and hydrodynamic lubrication ($\lambda > 3$), and the transition between the different lubrication states.

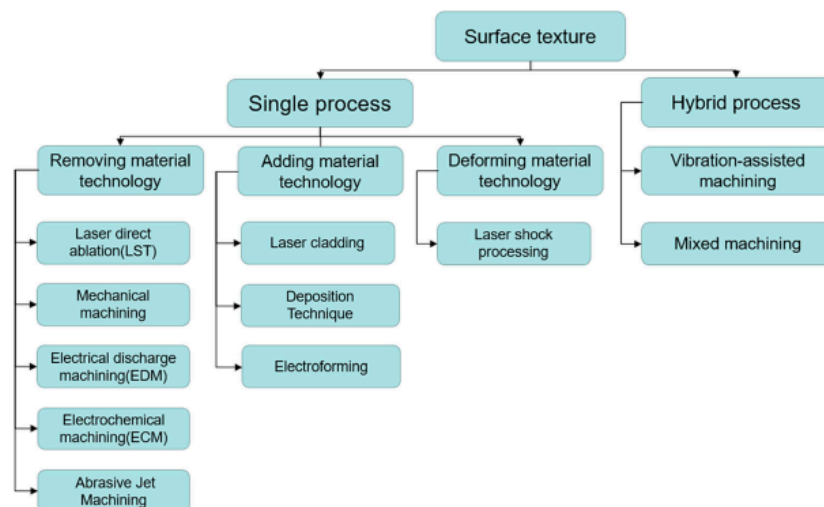


Figure 3. Classification of various texture processing methods [64].

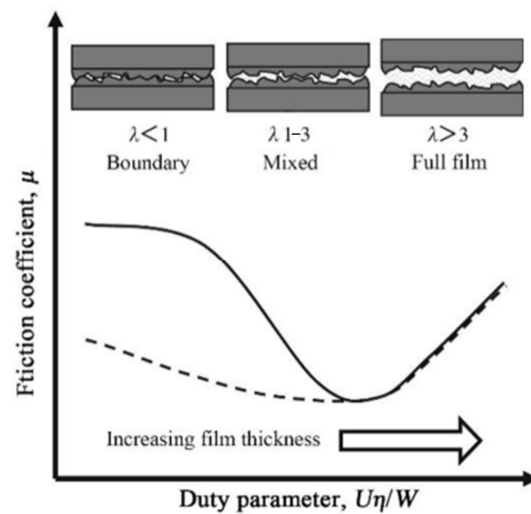


Figure 4. Stribeck curve of lubricants [69].

3.1.1. Hydrodynamic Effect and Cavitation Effect

No matter the type of textured surface, it is a combined micro-structure of convex and concave, through surface-molding technology. In the hydrodynamic lubrication and mixed lubrication state, the main lubrication mechanism is the hydrodynamic effect and cavitation effect [70]. Hamilton [65] found that micro-irregularities on the surface can improve the bearing capacity of the lubricant film. The micro-irregularities form a convergent wedge on their leading edge, thus generating additional hydrodynamic pressure on the lubricant film. The divergent wedge on the trailing edge causes a cavitation phenomenon, which restrains the generation of negative lubricant film pressure. Thus, the asymmetric pressure distribution occurs in the lubricant film, and the bearing capacity of the lubricants is improved, further separating the two friction surfaces with relative motion, as shown in Figure 5 [65] and Figure 6 [71]. Studies have shown that the hydrodynamic lubrication performance of the surface texture is affected by the shape [72], depth–diameter ratio [73], area ratio, relative position change [74], the contact mode change in the friction pair (line contact, surface contact) [75], etc.

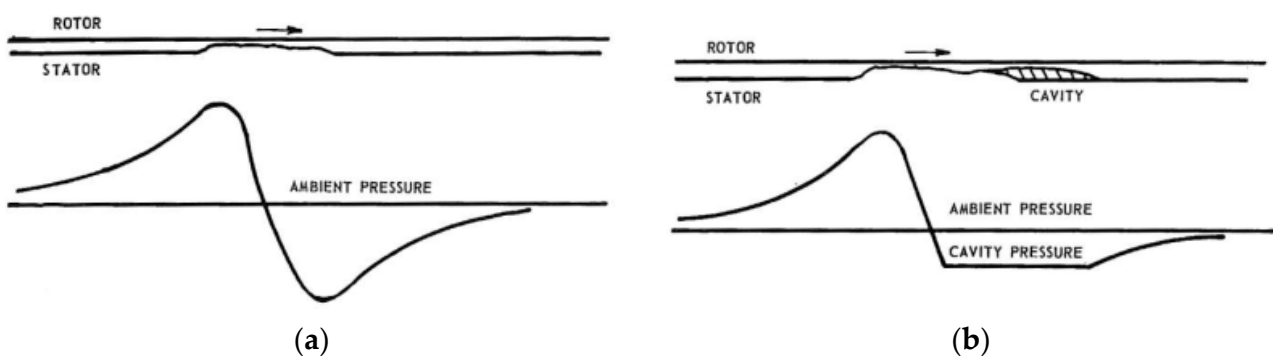


Figure 5. Sketch of idealized surface asperity and associated general pressure profile [65]: (a) no cavitation occurs; (b) cavitation occurs.

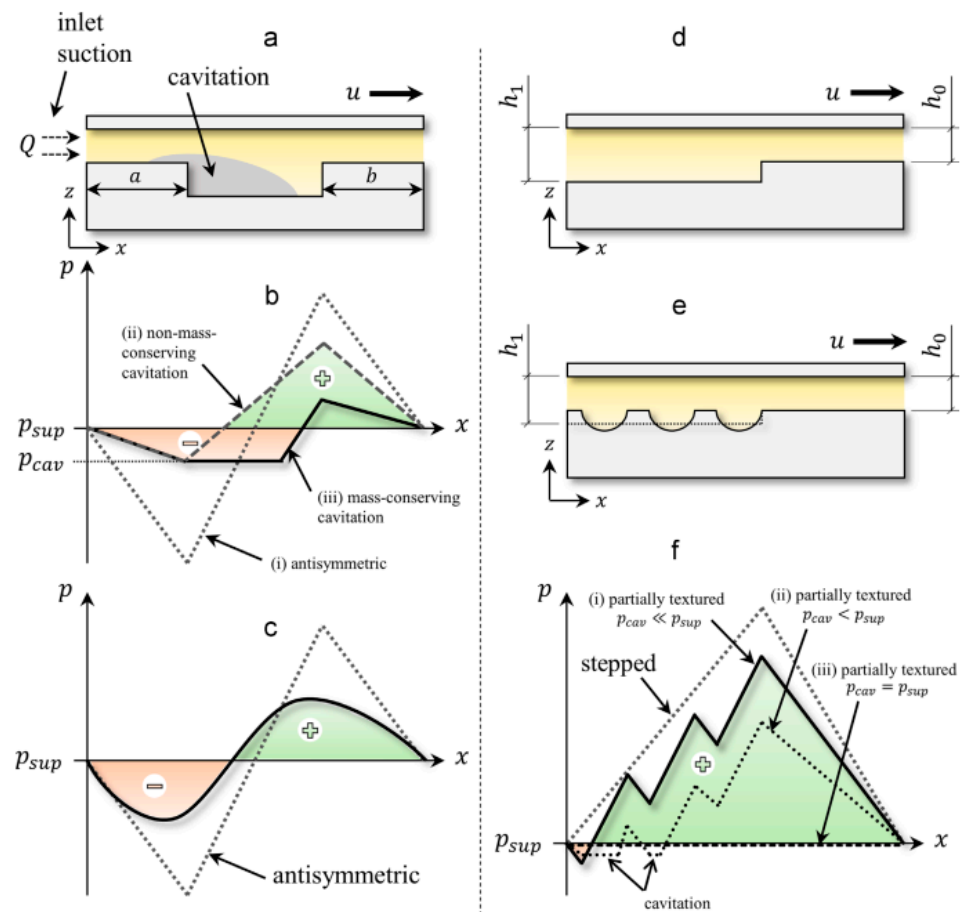


Figure 6. Mechanism of the hydrodynamic effect and cavitation effect of the surface texture under the fluid lubrication condition [71]: (a) single texture cell; (b) typical pressure distribution over a single texture with cavitation; (c) typical pressure distribution over a single texture with inertia effects; (d) stepped slider; (e) partially textured slider; (f) typical pressure distributions over a stepped and partially textured slider.

3.1.2. Secondary Lubrication Effect

In the boundary lubrication state, the lubrication mechanism mainly manifests as a secondary lubrication effect. The schematic diagram is illustrated in Figure 7 [64]. A surface texture of any shape can always form a concave space that can store more lubricant than a smooth surface [70,76,77]. As the friction process progresses, the lubricant between the friction surfaces decreases gradually, due to the friction contact, and the friction coefficient and surface temperature both rise. The resulting thermal expansion effect releases the solid lubricant stored in the concave space in the textured surface, and the polar molecules adsorbed on the friction surface form a boundary lubrication film with different properties from the lubricating medium, which effectively prevents direct contact between the friction surfaces, and achieves secondary lubrication [70,76,78].

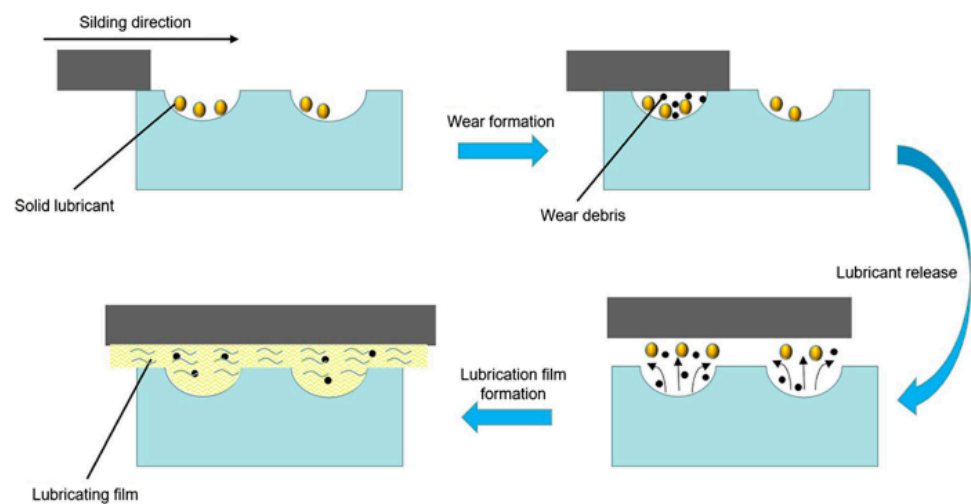


Figure 7. Mechanism of the secondary lubrication effect of the surface texture under the boundary lubrication condition [64].

3.1.3. Wear Debris Storage

In the dry friction state, the main lubrication mechanism is the storage of wear debris. With the relative movement of the friction pairs, wear debris is produced, and forms furrows on the contact surface, damaging the surface topography [79]. The working mechanism of the surface texture mainly includes the storage and containment of grinding particles and grinding chips. The secondary wear on the matrix, caused by high friction and wear due to the furrowing effect, can be reduced [80], as shown in Figure 8.

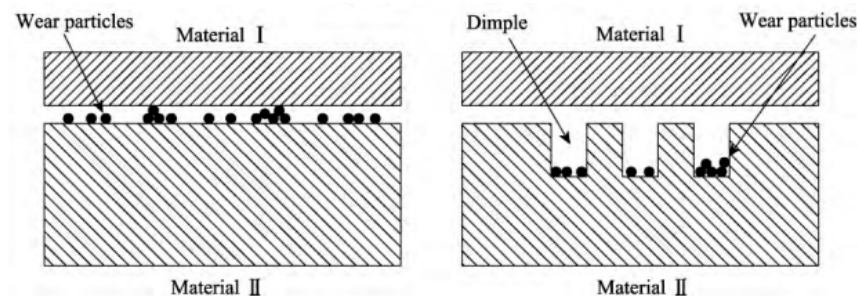


Figure 8. Mechanism of wear debris storage of the surface texture under the dry friction condition [80].

3.2. Texture Shape

As shown in Figure 9, scholars believe that the introduction of a micron or nanometer texture on the surface of key friction pairs can reduce the friction coefficient, reduce wear, and improve the friction and wear characteristics of friction pairs [65,71,81,82]. There are many common surface micro-texture processing methods [64], including laser surface texturing (LST) [82–84], electrochemical machining [85], micro-grinding [86], milling [87], electrical discharge machining (EDM) [88], abrasive jet machining [89], electroforming [90], and hybrid processing methods [91].

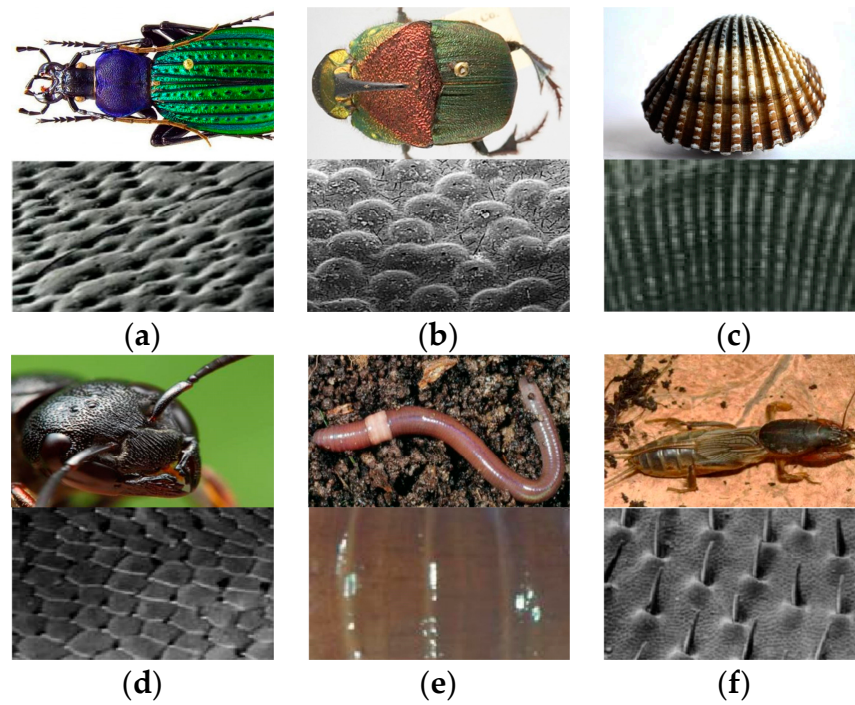


Figure 9. The surface structure of natural organisms: (a) *Stenocara*; (b) dung beetle; (c) shell; (d) ant; (e) earthworm; (f) mole cricket.

The shape categories of surface micro-texture include pits, convex bodies, grooves, and scales. Inspired by the microscopic appearance of the body surface of the natural organisms in Figure 10, the specimens with surfaces of hemispherical, elliptical, and triangular pits are processed, and tested for their tribological properties [92–95]. Based on the body surface of organisms, scholars have associated and designed some optimized and non-traditional micro-pits with different textures [96–98], shown in Figure 11. At the same time, it has been found that the combination of pits and grooves could also improve the effect of friction reduction and resistance, utilizing the texture morphology of the shell surface [99–101].

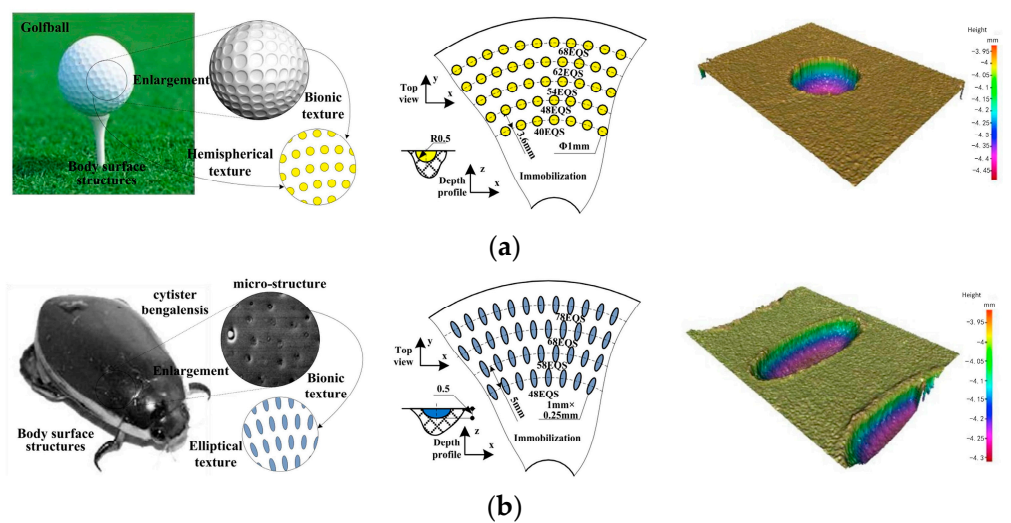


Figure 10. Cont.

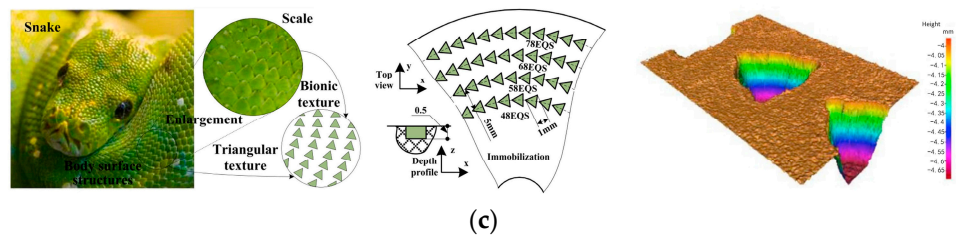


Figure 10. Friction surfaces with different bionic pit structures [92]: (a) hemispherical pits on the surface of a golf ball; (b) elliptical pits on the shell surface of a dung beetle; (c) triangular pits on the skin surface of a snake.

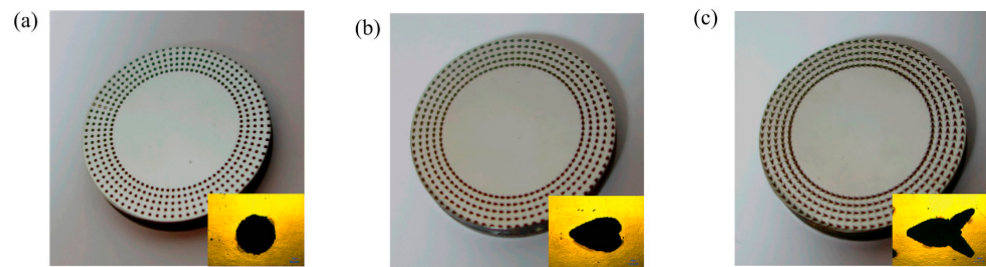


Figure 11. Photographs of disks with different pit shapes [98]: (a) circular; (b) bullet; (c) fish shape.

The micro–nano structure of the epidermis of the shark and *Phrynosoma cornutum* could inhibit the influence of turbulence. Figure 12 [102,103] and Figure 13 [104] simplify the scales into triangular, rectangular, arc-shaped, and trapezoidal groove units, which have a certain anti-friction effect. Earthworms can shuttle back and forth in the soil without being contaminated or worn by the soil, relying on the combined action of their surface groove texture, and mucus [105–107]. Due to its daily activities in the water, the relative angular velocity between the shell and gill cap of the water snail may inevitably lead to wear and tear at the interface between the shell and operculum [108]. However, the superimposed rings are concentrically distributed on the surface, which can generate hydrodynamic lubrication. The drag reduction mechanism of the groove, combining geometry and fluid mechanics, is revealed, theoretically and experimentally, in Figure 14 [109]. Biological morphology in nature not only has two types of pits and grooves. In Figure 15 [110], there is also a surface convex structure, and the wings of the dragonfly have a convex texture. There are also many shapes of surface convex bodies, including hemispherical, square, rectangular, cylindrical, and conical [110,111]. These also provide ideas for the textured-surface friction pairs.

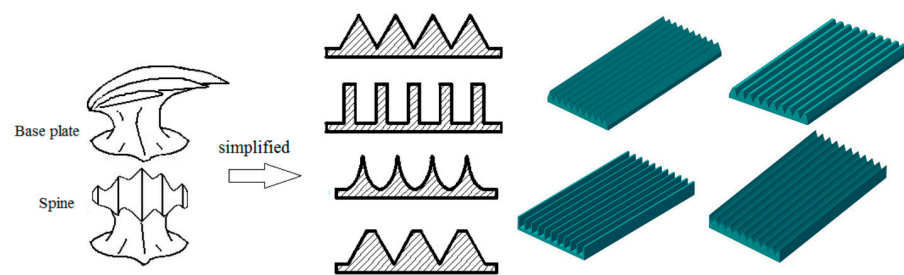


Figure 12. Different groove textures in shark scales [102,103].

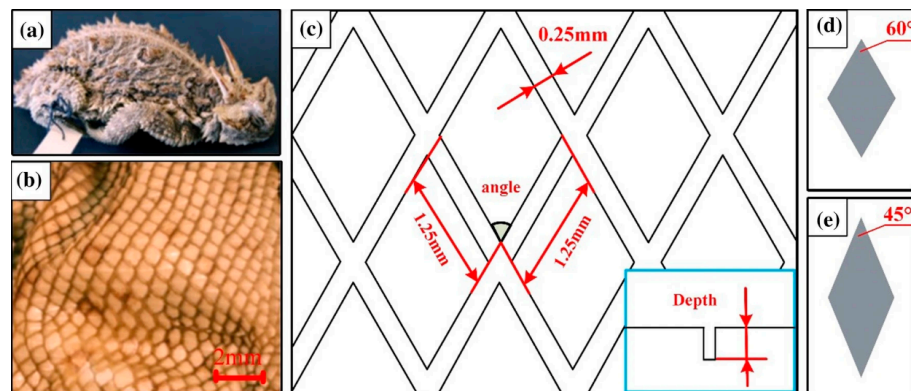


Figure 13. Scale micro–nano structure of the *Phrynosoma cornutum* epidermis [104]: (a) *Phrynosoma cornutum*; (b) the ventral scale structure; (c) schematic diagram of the bionic rhombic texture; (d) the rhombic textures of 60°; (e) the rhombic textures of 45°.

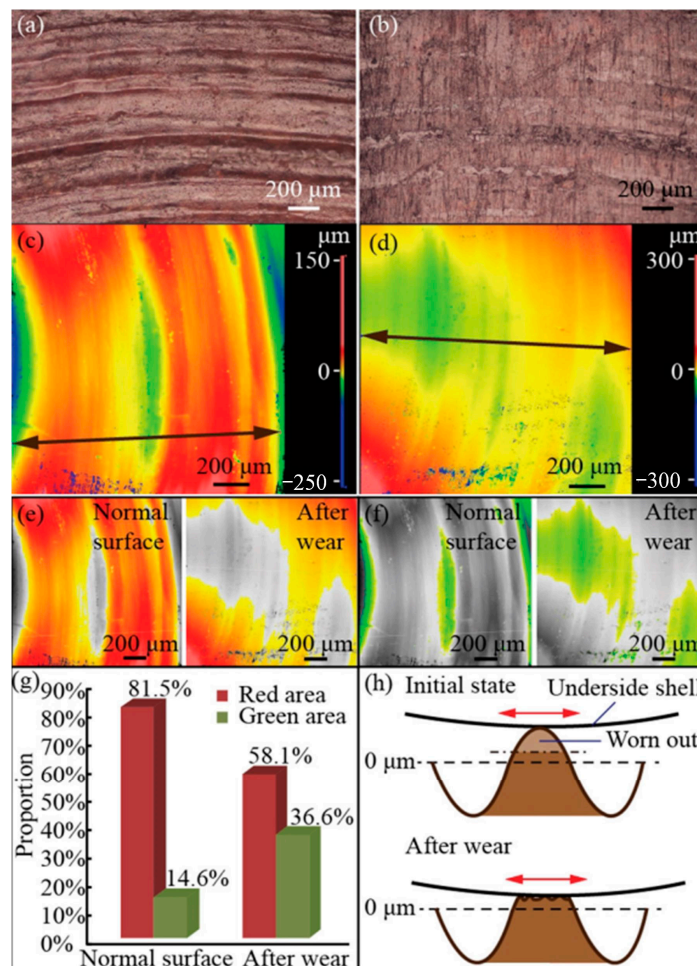


Figure 14. Tribological mechanism of water snails [109]: (a) morphology of the operculum of a fresh snail specimen; (b) morphology of the wear traces of the operculum after the dry friction experiment; (c) surficial topography of the operculum before the dry friction experiment; (d) surficial topography of the operculum after the dry friction experiment; (e) extraction of the red area (0–25 μm) before and after the dry friction experiment; (f) extraction of the green area (–5––25 μm) before and after the dry friction experiment; (g) bar graph of the proportion of red and green area before and after dry friction; (h) schematic illustration of the wear caused by dry friction for one micro-ridge.

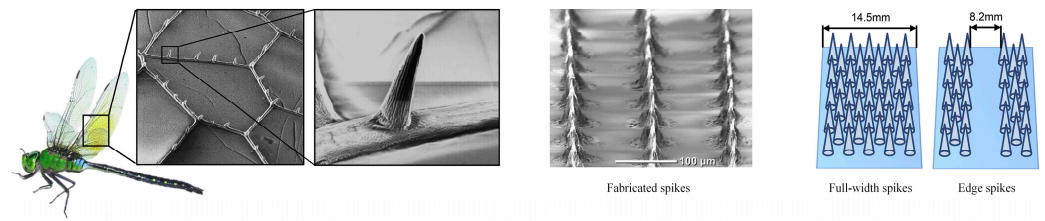


Figure 15. Imitation dragonfly convex-texture surface [110].

In addition, as shown in Figure 16, some natural organisms also secrete a lubricating medium to achieve friction reduction [107,108,112–116]. For example, human joint friction performance mainly comes from synovial fluid. The synovial fluid is mainly composed of hyaluronic acid (HA), mucin, glycoprotein, and brush components [113]. These macromolecules in synovial fluid have a high hydration level. Brasenia and papaya seeds contain a natural nano-cellulose material, with a significant ability to reduce friction [108,114,115]. Table 4 shows the friction and wear mechanism of different biological structure shapes.

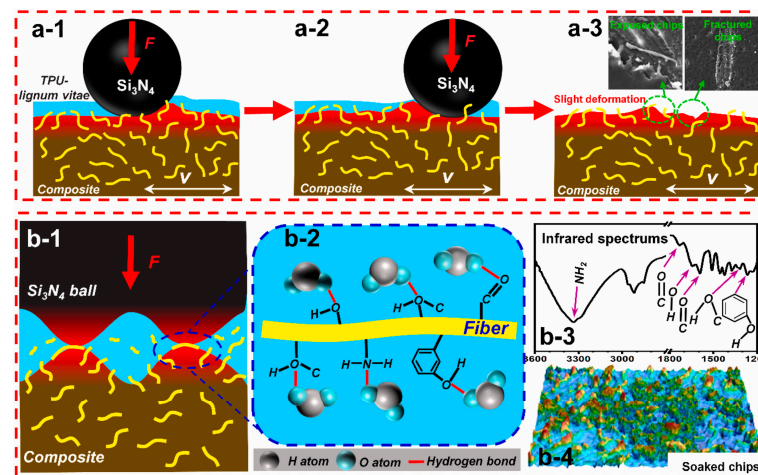


Figure 16. Schematic illustration for the mechanism of friction and wear [107]: (a-1–a-3) TPU composite; (b-1–b-4) lubricating mechanism of the lignum vitae at the contact interface.

Table 4. Tribological mechanism of different bionic micro-textures.

Organism/Tissue	Shape-Texture	Function	Mechanism	Reference
Snake	Triangular pit texture	Anti-friction	Reduce contact area	[92]
Golfball	Semi-spherical pit texture	Anti-friction	Reduce contact area	[92]
Dung beetle	Elliptical pit texture	Anti-friction	Reduce contact area and store lubricating oil	[92,95]
Shell	Groove texture	Anti-wear	Provide hydrodynamic lubrication	[95,96]
Phrynosoma cornutum	Diamond texture and lubricant	Anti-friction	Form a lubricating film	[104]
Shark	Groove texture and lubricant	Anti-friction	Change turbulent pressure and increase the viscosity	[102,103]
Dragonfly	Micro-spike texture	Anti-drag	Form a gas-phase region and suppress circulation flow and whirling	[110]
Earthworm	Groove texture and mucus	Anti-drag	Reduce contact area and viscous friction	[105,106]
Water nail	Groove texture	Anti-friction	Provide hydrodynamic lubrication	[109]
Lignum vitae	Fiber, conduit, and resin	Anti-friction	Fiber-reinforced, emulsion-forming	[107,112]
Joint	Synovial fluid	Anti-friction	Hydration	[113]
Brasenia	Mucus	Anti-friction	Hydration	[114,115]
Papaya seeds	Seed mucus	Anti-friction	Hydration	[108]

3.3. Equivalent Diameter

One way to increase the bearing capacity of the friction surfaces is to produce a better hydrodynamic pressure. Recent studies have shown that microscopic textures, such as pits, can achieve better hydrodynamic effects. In addition, the rapid development of laser technology [117] and diamond-like carbon (DLC) coating technology [118] provides good technical support in the fabrication of micro-structures. Therefore, based on flexible and accurate micro-manufacturing technology, the friction performance and bearing capacity of a non-smooth bionic texture can be further improved by optimizing the size parameters of the pits. One of the important size parameters of the pit is the diameter. It is worth mentioning that the circular pit is easy to manufacture, and low cost. It is the most popular texture pattern, but because the shape of the pit also has various styles, such as square, this section discusses the equivalent diameter of the texture.

3.3.1. Study on the Critical Value of Pit Equivalent Diameter

The research shows that the friction process is mainly divided into two stages. In the early stage of running-in, the friction coefficient fluctuates obviously. In the second stage, the texture pattern and the smooth pattern are stable. As shown in Figure 17, the experimental data of Sun [119] show that the wear volume in the first stage accounts for about 60% of the total friction process, and the wear amount in the steady friction process in the later stage of the running-in is less. The surface texture with a relatively small diameter may improve the friction performance.

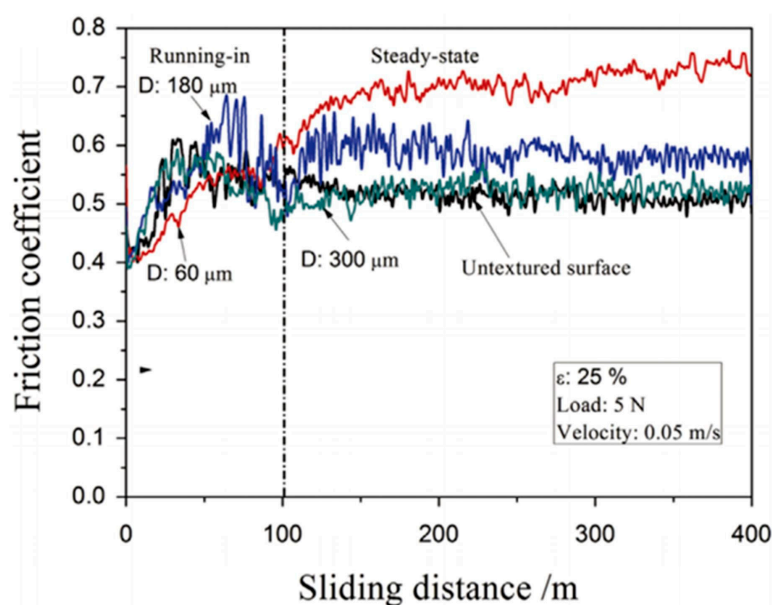


Figure 17. The variations in the friction coefficient of the untextured and textured surfaces with different dimple diameters, at a normal load of 5 N, and the sliding distance of 400 m [119].

Some studies have found that the diameter of the pit is not linearly related to the friction coefficient and the hydrodynamic pressure. As shown in Figure 18 [119], there is a critical value for the contact width. If the diameter is greater than or less than the contact width, the lubricant film thickness and the bearing capacity will change significantly [120–122]. A pit diameter which is equal to, or less than, the contact width will reduce the friction coefficient, while the pit diameter which is much larger than the contact width will increase the friction coefficient. This contradicts the experimental data of Sun [119] mentioned before. We believe that it is because the sample point selection methods of the two are different, and the number of samples is different. The selected sample diameter of Sun's study [119] was much larger than the contact width, resulting in a linear correlation.

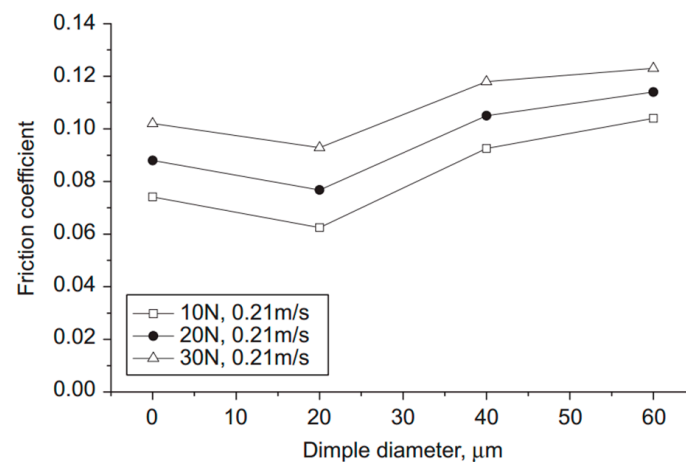


Figure 18. The effect of the dimple diameter on the friction coefficient at the sliding speed of 0.21 m/s [119].

3.3.2. Study on Micron Level Size Diameter

The size of the micron scale is mainly distributed between 10 μm and 1000 μm . Under the same conditions, the lubrication effect will be better with the increase in the radius of the pit. As shown in Figure 19, in order to better show the friction performance, Yin [123] proposed the average dimensionless friction force F_M . The experimental results show that the radius increases from 20 mm to 60 mm, resulting in a 27% reduction in F_M , indicating that the increase in the pit radius has a significant positive effect on the lubrication. In the case of low speed and high speed, the influence of the diameter of the micro-texture on the friction performance is not obvious, but at the medium speed, the influence is obvious, the correlation is not linear, and there is an optimal size. Studies have shown that the best size is about 40 μm in the case of linear motion [124].

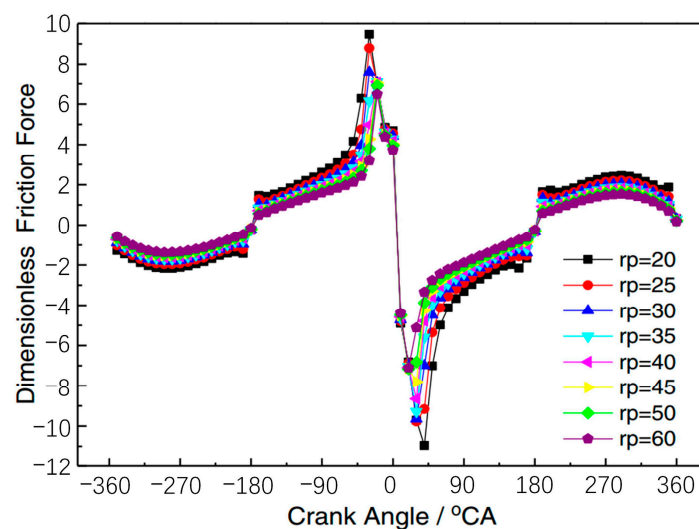


Figure 19. The dimensionless friction force with $S_p = 0.35$ and $h_p = 4.8 \mu\text{m}$ for different dimple radii r_p [123].

It should be emphasized that different motion modes and directions also lead to different friction properties. Texture can be constructed on the coating by combining DLC and laser technology. The groove texture is created using this method. When the groove is orientated along the sliding direction, it is similar to the larger texture, and the friction wear rate is higher. However, when it is perpendicular to the sliding direction, the friction and wear properties are good [125,126].

The motion mode of the swash plate and the other structures of the axial piston pump is circular motion, and the friction law of linear motion cannot be applied directly.

Therefore, some scholars have focused on the influence of the micron texture radius on the friction performance of circular motion. Tang [127] optimized the mechanical parameters of the texture based on the multi-objective agent model. Figure 20 shows that there is no linear relationship between the diameters and frictional properties under circular motion, but the optimal solution is between 15 μm and 18 μm , which is similar to the rule of linear motion of the former.

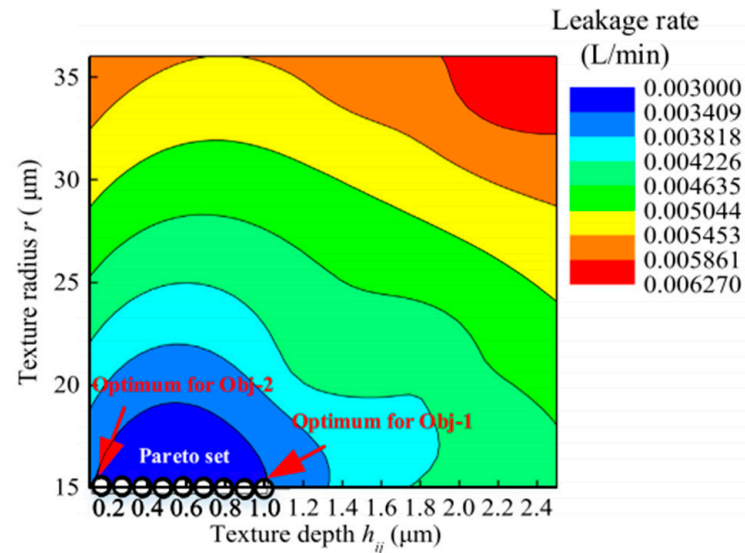


Figure 20. Objective-function contours, based on a comprehensive sampling of the texture design [127].

It is worth mentioning that the lubrication mechanism of pits is different under the conditions of lubrication and dry friction [128,129]. Under dry friction conditions, the texture diameter of the micron texture has no significant influence on the friction performance. However, as shown in Figure 21, with the increase in diameter, the abrasive wear turns to adhesive wear, leading to the reduction of wear [130].

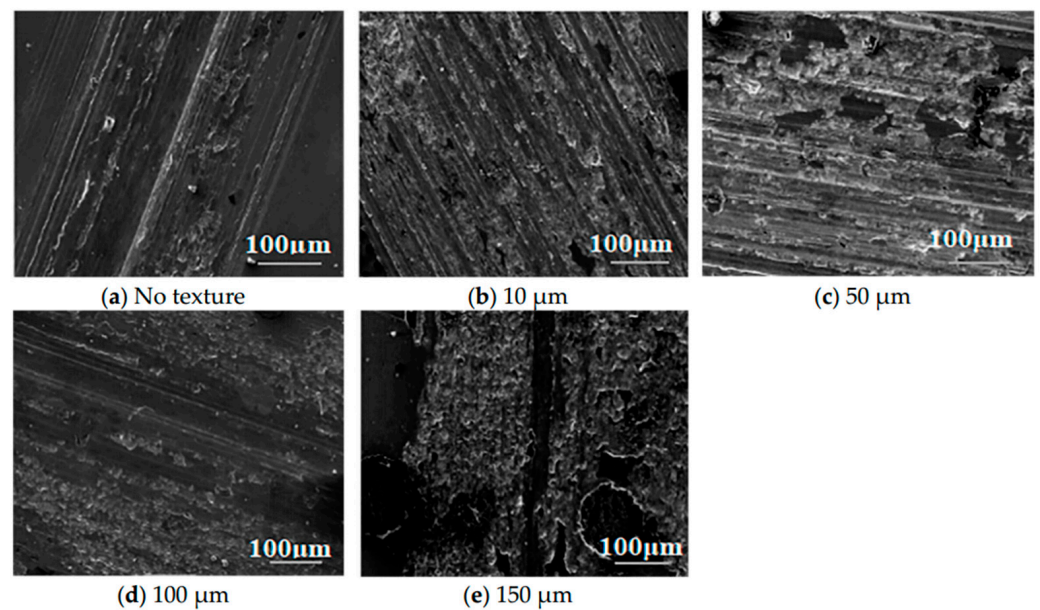


Figure 21. Microscopic morphology of the wear scars of different pit diameters, under dry friction [130]: (a) no texture; (b) 10 μm ; (c) 50 μm ; (d) 100 μm ; (e) 150 μm .

3.4. Depth

The depth of the texture is the main factor affecting the hydrodynamic lubrication performance of the surface-textured fluid. Designing the most suitable geometric parameters for the surface texture can make the textured surface obtain the optimal tribological properties and lubrication performance. Through the study of biological external morphology, surface morphology, internal structure, and other structural characteristics, scholars have explored the physical nature of different biological surface morphologies, and have applied it to the design and development of the surface texture, providing new ideas and methods for the design and preparation of mechanical parts. At the same time, in the design of surface bionic texture, we should not blindly pursue the reproduction of biological structures, but need to innovate and optimize the design in imitation, to obtain the optimal design parameters. Through the above analysis, the geometric parameters of different types of bionic surface textures are summarized, as shown in Table 5.

Table 5. Geometric parameters of the bionic surface texture.

Bionic Surface Texture Type	Bionic Object	Bionic Size/mm
Natural structure	Raindrop ellipsoid structure	1~10
Surface of plants	Green radish surface	0.01~0.1
	Lotus leaf surface	0.01~0.1
Surface of insects	Dung beetle chest back plate pit	0.01~1
	Beetle head bump	0.01~1
	Pill worm body surface ripple	0.01~1
Surface of terrestrial animals	Pangolin squama surface	0.1~10
	Snake scale surface	0.1~10
Surface of marine organisms	Shark skin	0.1~10
	Shell surface	0.01~1

3.4.1. Effects of Different Depths

Under fluid lubrication, the depth plays a decisive role in the thickness and bearing capacity of the lubricating film. When the depth is shallow, the thickness of the lubricating film will increase significantly, while, when the depth is deep, the thickness of the lubricating film will decrease locally [131]. This conclusion is consistent with Kaneta's research [132].

The dynamic pressure generated in the fluid film between the two friction surfaces enhances the bearing capacity of the texture. The depth of the surface texture is an important geometric parameter affecting the hydrodynamic lubrication. The bearing capacity of the lubricant film will increase first, and then decrease, with the increase in depth. Scholars have verified the two-dimensional model and the three-dimensional model, successively. Sahlin [133] used knowledge of fluid mechanics to calculate the two-dimensional fluid domain between two parallel walls, with pits on the lower wall. The geometric structure is shown in Figure 22, and the pressure and streamline of the upper wall, with different Reynolds numbers and different pit depths, are compared. The calculation results for the upper wall pressure are shown in Figure 23. The results verify that the depth of the pit has a nonlinear relationship with the dynamic pressure-bearing capacity. As the depth of the pit increases, the pressure on the upper wall increases first, and then decreases. Han [134] used the computational fluid dynamics (CFDs) method to analyze the hydrodynamic lubrication characteristics of the micro-pit surface-sliding friction pair in three dimensions. In the case of different Reynolds numbers, the bearing capacity increases first, and then decreases, with the increase in the depth of the pit. The calculation results verify the two-dimensional analysis.

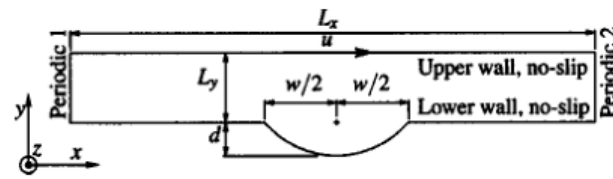


Figure 22. The fluid domain of the cylindrical geometry, including the geometrical parameters and boundary conditions [133].

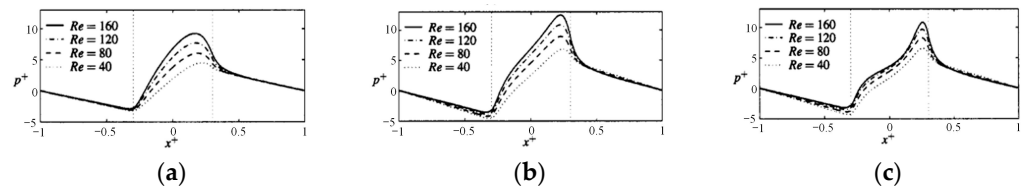


Figure 23. Upper-wall pressure distribution for the cylindrical geometry, with $w^+ = 0.30$ [133]: (a) $d^+ = 0.25$; (b) $d^+ = 0.75$; (c) $d^+ = 1.25$.

The vorticity and recirculation of the fluid in the texture depend on the depth of the texture, and increase with the depth of the texture. In 2018, Vilhena [94] used the CFD method to perform a three-dimensional analysis of the sliding friction pair on the surface of the semi-circular cavity. The geometric model is shown in Figure 24. The streamlines at different depths in the cylindrical cavity are shown in Figure 25. Through the observation of the streamlines at different depths in the cylindrical cavity, the dynamic performance of the fluid is understood. As the depth of the semi-circular cavity increases, a vortex is formed in the cavity, with a closed contour.

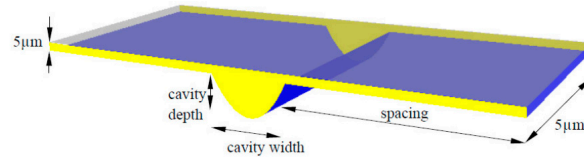


Figure 24. Geometrical parameters for the cylindrical geometry [94].

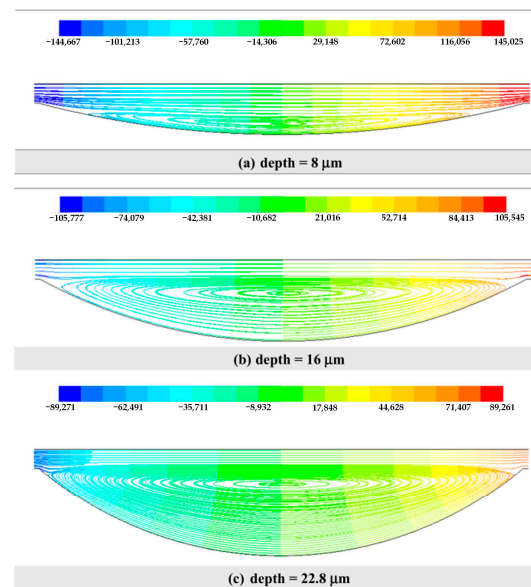


Figure 25. Streamlines (colored according to static pressure [Pa]) in the cylindrical geometry for different values of depth, where the cavity width = $128 \mu\text{m}$, spacing = $500 \mu\text{m}$, $u = 0.1 \text{ m/s}$ [94]: (a) depth = $8 \mu\text{m}$; (b) depth = $16 \mu\text{m}$; (c) depth = $22.8 \mu\text{m}$.

Different texture shapes show different friction characteristics under different depth conditions. For example, Wang [96] compared the friction properties of six different bionic shell-surface textures. As shown in Figure 26, the composite structure of the grooves and pits shows a better wear reduction effect, and the optimal depth parameters are obtained under different area ratios.

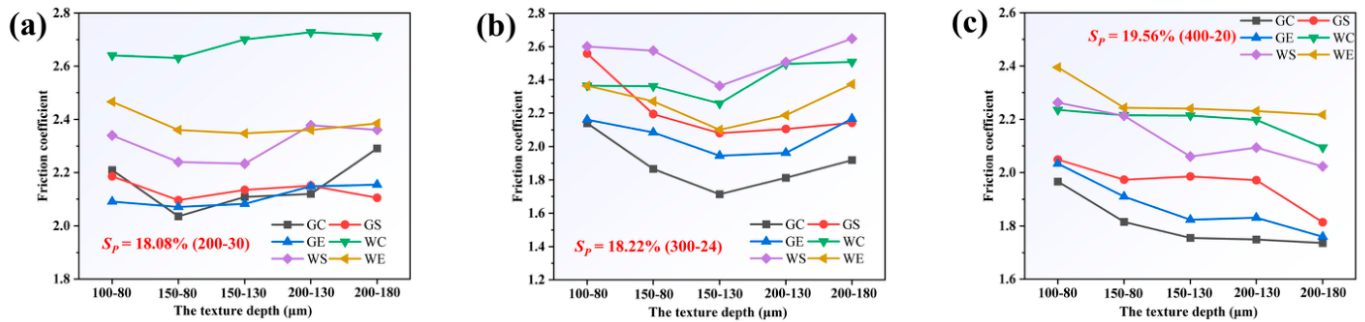


Figure 26. The impact of the texture depth on the friction coefficient of the six texture shapes at different densities [96]: (a) $S_p = 18.08\%$; (b) $S_p = 18.22\%$; (c) $S_p = 19.56\%$ ($U = 4000$ r/min, $h = 16$ μm).

3.4.2. The Influence of the Different Depth-to-Diameter Ratio

For different working conditions, there is also an optimal ratio of texture depth to diameter [135]. Regarding the diameter and the depth of the texture, it is not a case of the larger, the better. When the depth-to-diameter ratio is high, to a certain extent, it is easy for micro-vortexes to form in the pit, which affects the hydrodynamic lubrication. When the diameter is too large, the pit can be approximated as a flat plate, unable to produce a fluid hydrodynamic effect, and thus losing meaning.

In 2014, Kim [136] used a pin-on-disk friction test bench to study the effects of surface texturing on the frictional behavior, and the test flow chart is shown in Figure 27. A comparative test is performed at two depth-to-diameter ratios of 0.14 and 0.3. It is concluded that under high lubrication parameter values, the friction coefficient of a small depth-to-diameter ratio is lower than that of a large depth-to-diameter ratio. The test results are shown in Figure 28.

The spherical bump texture effectively improves the tribological properties of water-lubricated friction pairs. The texture of the spherical bulge reduces the contact area between the friction pairs, thereby reducing the adhesion effect. The spherical convex texture changes the streamline between the friction pairs, and increases the flow rate of the water so that the debris cannot be retained on the worn surface, thereby reducing abrasive wear. The spherical convex structures with different depth-to-diameter ratios have different contact areas of friction pairs, so their tribological properties are different. In 2019, Hu [137] prepared a spherical convex surface on the bearing surface. Under water lubrication conditions, it is concluded that a bearing with a small aspect ratio has the best friction performance.

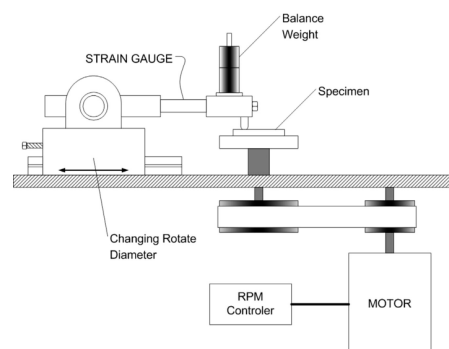


Figure 27. Equipment setup for the tribology test [136].

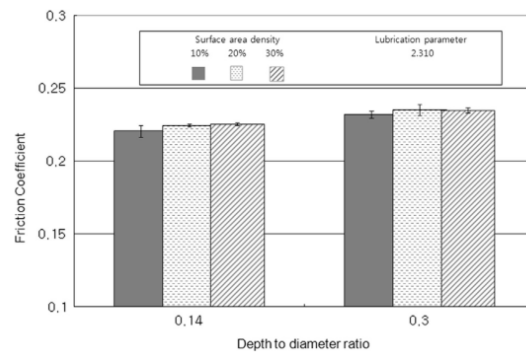


Figure 28. Comparison of the coefficients of friction from three different surface area densities, at a high lubrication parameter value, for two different depth-to-diameter ratios [136].

With the deepening of the research, some studies have shown that the optimal geometric size of the surface texture will be affected by the working conditions, lubrication methods, and other factors. In 2017, Li [138] established a lubrication model of micro-dimple array friction pairs based on Navier–Stokes equations, using a three-dimensional CFD simulation method. The effects of different texture area ratios and depth-to-diameter ratios on the average lubricant film bearing capacity and friction coefficient were analyzed at Reynolds numbers 5, 50, and 250. As shown in Figures 29 and 30, the average lubricant film bearing capacity increases first, and then decreases, with the increase in the depth–diameter ratio. At low Reynolds numbers, the friction coefficient decreases with the increase in the aspect ratio. At high Reynolds numbers, the friction coefficient decreases first, and then increases, with the increase in the aspect ratio.

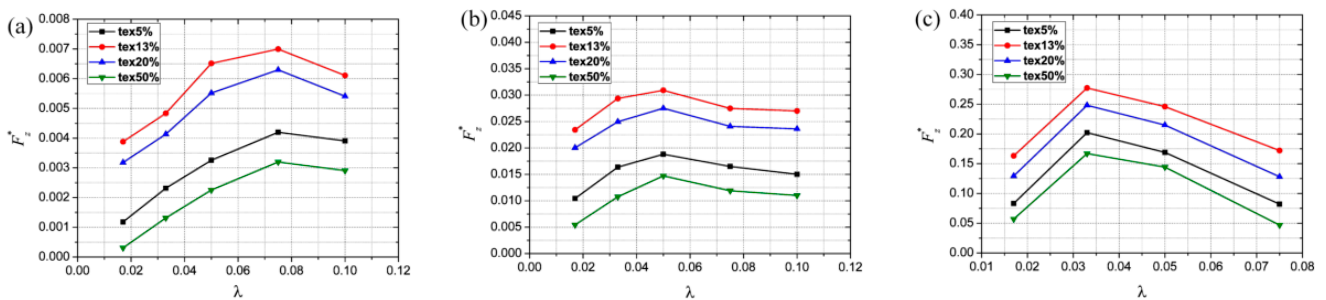


Figure 29. Effect of the texture density and depth-to-diameter ratio on the dimensionless average film-carrying force [138]: (a) $Re = 5$; (b) $Re = 50$; (c) $Re = 250$.

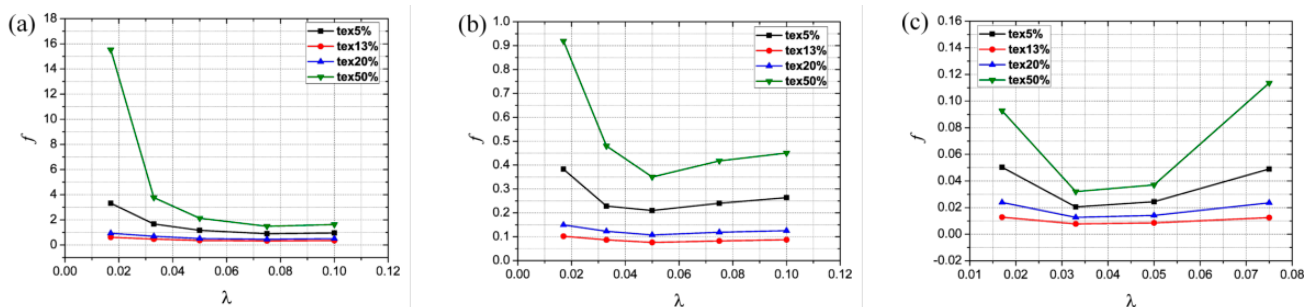


Figure 30. Effect of the texture density and depth-to-diameter ratio on the friction coefficient [138]: (a) $Re = 5$; (b) $Re = 50$; (c) $Re = 250$.

3.5. Arrangement

The arrangement of the texture is also one of the factors affecting the surface friction. It can be mainly based on the area ratio and the rules of arrangement. It is not the case that the higher the number of surface micro-textures, the better. It is necessary to select the best arrangement for reducing friction, through simulation or experimental comparison.

3.5.1. Texture Area Ratio

The area ratio of the texture is determined by the density of the texture arrangement, which is one of the vital factors in improving the tribological performance. On one hand, the surface texture will increase the surface roughness and actual contact pressure, which will lead to friction and wear, and increase the coefficient of the friction. On the other hand, the texture will act as a reservoir for storing lubricants, which can improve the lubrication condition, and reduce the friction coefficient [139].

Shimizu [140] produced the surface texture of a brass plate, with the surface texture of 40%, 25%, and 10% respectively, in the condition of dry friction, as shown in Figure 31. It can be seen that the friction coefficient is the lowest, and the wear is the lowest, when the area ratio is 40%. Similarly, Hu [141] made micro-pits with different area ratios on the surface of Ti-6Al-4V, and carried out a series of experiments under dry friction and molybdenum disulfide lubrication conditions. The results show that the friction performance is much better when the area ratio is 44% than when it is 13% or 23%, or when there is no microstructure. Meng [142] carried out friction and wear experiments on laser-textured surfaces under dry friction and W-S-C solid lubrication conditions, as shown in Figure 32. In the case of dry friction, the friction coefficient decreases with the increase in the groove area ratio. After solid lubrication, the groove area ratio maintains a good friction performance until 9%. Li [143] prepared surface textures with different area ratios on No. 45 steel, and found that the wear condition is the lightest when the area ratio of the texture is 8.1% under dry friction and oil deficiency conditions. Under the action of dry friction, the area ratio of the surface texture directly affects the contact area, and the capture of wear particles. In a certain range, the larger the area ratio, the smaller the friction coefficient.

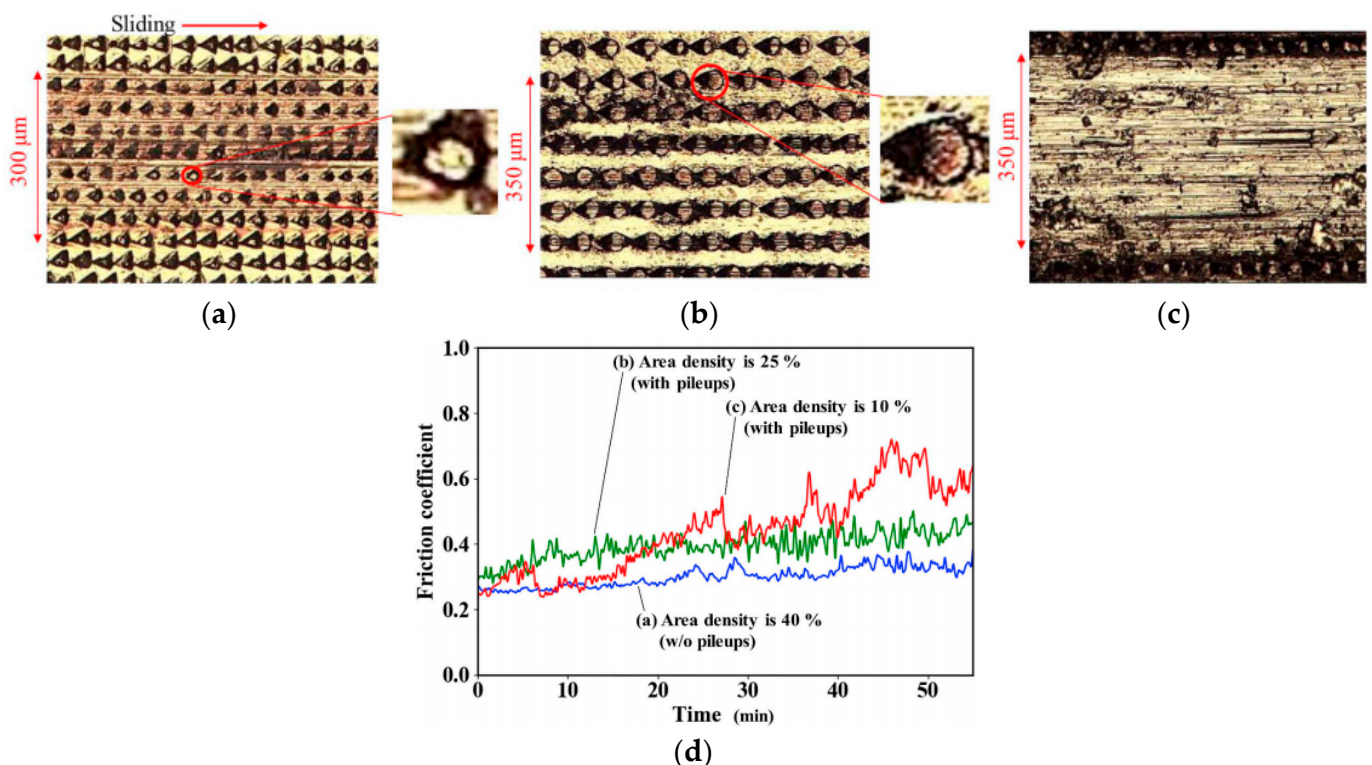


Figure 31. Micrographs of the wear trajectories on the surface of an advanced technical texture [140]: (a) with an area ratio of 40%; (b) with an area ratio of 25%; (c) with an area ratio of 10%; (d) with the effect of the area ratio on the friction coefficient.

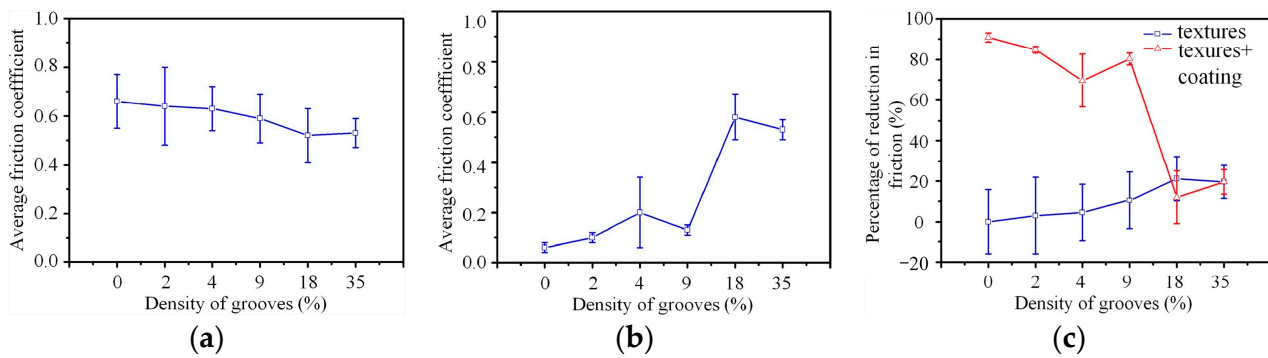


Figure 32. Comparison of different friction coefficients of the surface texture under dry friction and solid lubrication conditions [142]: (a) the average friction coefficient under dry friction; (b) the average friction coefficient under W-S-C solid lubrication; (c) the magnitude of the decrease in the friction coefficient between the surface texture and the non-surface texture.

In Hu's study [137], using a QSn7-0.2 bearing under the same pressure and speed, the friction and wear tests were carried out by fluid lubrication on a non-textured, quarter ball, one-third ball, and one-half ball, at the area rate of 25%, 31%, 38%, and 44%, respectively. As shown in Figure 33, the results show that the surface texture with an area rate of 38% has the lightest wear at three different sphere heights, and the wear is more serious when the area rate increases to 44%. Zhang [139] studied the relationship between the average friction coefficient and the texture area ratio, under the condition of a 3 N load and 0.69 m/s sliding speed. It is concluded that the average friction coefficient is the smallest when the texture area ratio is 15%, and then an increase in the area ratio will lead to an increase in the average friction coefficient. Wei [144] obtained the optimum area ratio of the zither-shaped surface texture through simulation and friction lubrication experiments. Firstly, the maximum positive pressure and the maximum lubricant film bearing capacity are obtained via simulation, when the area ratio is 22.7%. Then, the adjacent area ratio is tested, to obtain the minimum friction coefficient for the surface texture area ratio of 22.7%. In fluid lubrication, if the area ratio of the surface texture is too low, it will not increase the pressure of the water film, resulting in an unstable water film, and poor lubrication. When the area ratio is too high, the texture is arranged too closely, which will hinder the formation of a continuous water film on the worn surface, and this will also lead to wear. Therefore, it is necessary to select the appropriate area ratio, according to different types of textures, to minimize friction and wear.

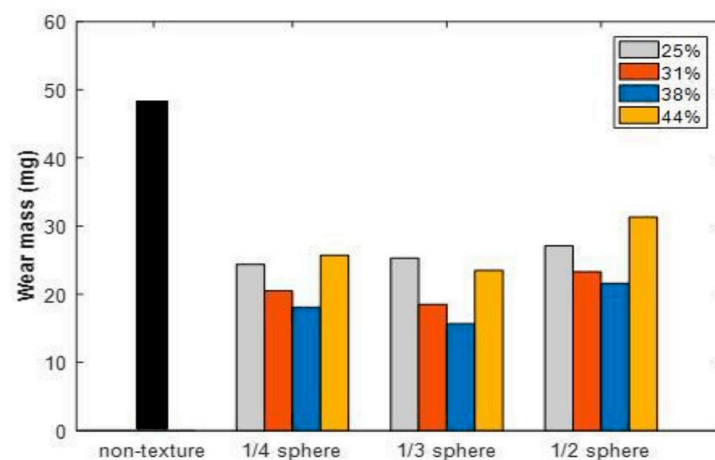


Figure 33. Attrition at different texture heights and area ratios [137].

In summary, according to the type of texture and lubrication conditions, the optimum texture area ratio of the typical texture is summarized, as shown in Table 6. Considering the different materials, it is also necessary to optimize the design for special cases.

Table 6. The optimum area ratio of different texture types.

Type	Lubrication	Density	References
Circular pit	Fluent	5–35%	[145,146]
Ellipse	Fluent	10.6–14.1%	[147]
Hexagon	Fluent	25%	[148]
Bulbous	Fluent	30–40%	[137]
Kite	Fluent	22.7%	[144]
Dimples	Dry	40%	[140]
Grooves	Dry	18–35%	[142]
Grooves	Solid	1–9%	[142]

3.5.2. The Arrangement of Texture

The main common arrangement forms are transverse arrangement, longitudinal arrangement, circumferential arrangement, staggered arrangement, and so on. The tribological properties of different arrangement modes will also cause great differences. Therefore, it is necessary to select the optimal arrangement form, by simulation or experiment.

The lubricating film pressure on the textured surface can be obtained by theoretical simulation, so that the anti-friction benefit of the surface texture can be analyzed based on the bearing capacity of the lubricating film, and the lubricating film thickness. Wang [149] used the method of the numerical solution to simulate the rectangular grooves of 90°, 75°, 60°, 45°, 30°, and 15°, and analyzed the simulation results. The results show that when the texture depth is less than 5 microns, the 75° and 90° grooves demonstrate a lower friction coefficient; when the groove depth is greater than 5 microns, the groove with a 60° arrangement shows the best friction performance and, at any depth, the groove with a 15° arrangement is the worst, followed by those with 30° and 45°. Wang [150] used the CFD method to simulate the lubricating film pressure of different arrangement surface textures. The main arrangement method is shown in Figure 34. The simulation results show that the staggered micro-pits have a better friction performance. Yi [151] established the finite element model of sliding bearings, and simulated the arrangement of the micro-texture. The results show that the influence of the micro-texture on the bearing characteristic coefficient is more obvious when the micro-texture is arranged circumferentially. Wang [152] used the numerical simulation method to study the friction performance of the micro-cylindrical pit texture, and simulated the offset rate of different texture positions. The results show that as the offset rate increases, the total pressure near each texture unit increases, and a more effective bearing capacity is obtained. The above shows that the arrangement of the micro-texture has a great influence on the friction performance, and that the circumferential arrangement and staggered arrangement can better improve the friction performance. This is because these two arrangements can make the lubricant produce an asymmetric pressure distribution, and improve the lubricating film bearing capacity.

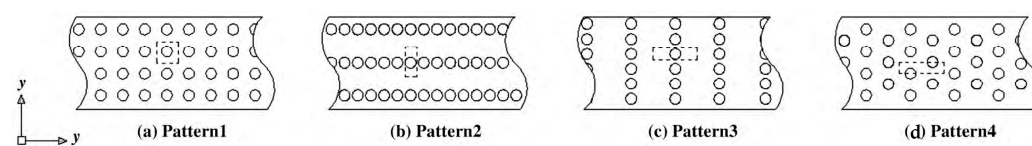


Figure 34. The four different arrangements of surface texture [150]: (a) regular; (b) transverse; (c) longitudinal; (d) staggered.

To improve the tribological performance of the bearing slider, Zhang [153] obtained the optimal friction performance of the slider when the texture is arranged in a micro-pyramid shape, via mathematical optimization. Schneider [154] carried out a one-way

sliding experiment on the laser-textured surface, and studied the influence of different texture arrangements on the surface sliding. The arrangements were hexagonally staggered, cubically staggered, and random, as shown in Figure 35. Finally, it was concluded that the friction coefficient of the hexagonal staggered shape was the largest. Under the condition of boundary lubrication, Yue [155] fabricated micro-textures parallel, perpendicular, and 45° to the sliding direction, and the friction coefficient was lower than that without texture. Antoszewski [156] found that the lubrication effectiveness depended on the shape, size, and mutual distribution of the texture's elements, and demonstrated the significant role of the relationship between the trajectory of motion and the texture mesh.

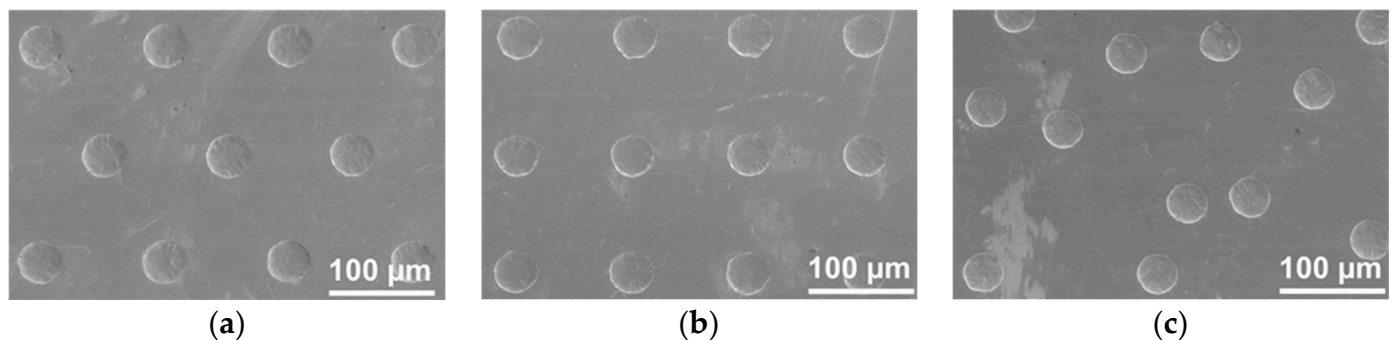


Figure 35. Three different permutations [154]: (a) hexagonally interlaced; (b) cubic; and (c) random permutations.

From the existing research, the reasonable arrangement of the surface texture can effectively improve the anti-friction performance. The same texture arrangement form and arrangement position are different, and the tribological performance is also quite different. Therefore, while referring to the theoretical research, it is necessary to consider the actual conditions, such as the lubrication state and the arrangement position of the texture.

3.6. Hardness, Microstructure, and Wettability in Texturing

During the process of processing textures (Figure 3), the laser, electricity, and cutting tool not only change the surface shape of the materials, but also have an impact on the hardness, microstructure, and wettability of the materials.

3.6.1. Hardness

The hardness change in the material surface during the process of manufacturing the surface texture is a key factor affecting the friction performance. LST has attracted much attention, due to its high flexibility, superior texture accuracy, and good controllability in the processing of surface texture [82]. Guo [157] used laser shock processing technology to fabricate the surface texture, and tested the hardness after processing. LST increased the hardness of the dents. This is due to the existence of tensile stress, which will affect the tribological behavior. Similarly, Garcia-Giron [158] has conducted similar research. After LST, the wear rate of an aluminum alloy could be reduced by seven times, due to the composite surface hardening and surface texture. After laser bionic texture treatment, Li [159] found that the micro-hardness of the microstructure in the bionic texture area was more than three times that of the untreated sample. Hussein [160] studied the effect of laser treatment on the mechanical properties, wear resistance, and Vickers hardness (HV) of an aluminum alloy. The results showed that the wear rate of the sample with circular grooves after laser treatment was lower than that of the sample without grooves.

The ultrasonic vibration-assisted turning (UVAT) process is also one of the effective methods to improve tribological properties. Amini [161] prepared micro-void arrays on the surface of Al7075-T6 using UVAT, and evaluated the effect of the surface hardness of the UVAT process on the surface microstructure and wear rate, via a hardness test. The results showed that, due to the unique properties of the micro-voids generated on the

surface by the UVAT process, the three-dimensional parameters of the surface geometric properties and roughness could be improved, and the surface hardness increased. These factors increased the wear resistance, and reduced the friction coefficient.

Ji [162] compared the wear resistance of the surface texture prepared using EDM under different working fluids. The four types of samples were the sample prepared with deionized water (named WMS), the sample prepared with kerosene (named KMS), the sample prepared with water-in-oil (named WOMS), and the non-textured sample (named SS). The surface micro-hardness of the different working fluids was obtained, as shown in Figure 36. It can be seen from the figure that the surface hardness of the WOMS is the highest. This is because the cooling rate of the WOMS working fluid is faster, which refines the surface grains. The research results of the relevant literature show that the internal properties of the material changed during the preparation of the surface texture, so the hardness changed, and affected the wear resistance.

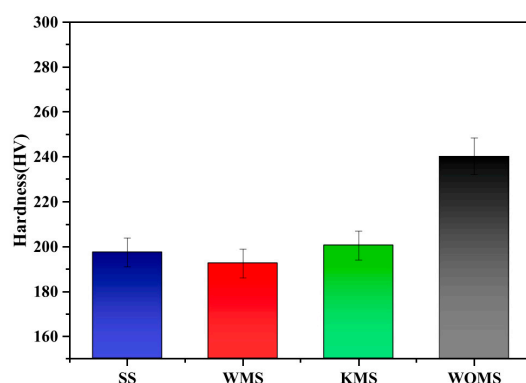


Figure 36. Average surface hardness of the different samples [162].

3.6.2. Microstructure

In the process of manufacturing surface textures, the internal structure of the material changes slightly, which will directly affect the friction performance of the material. Syed [163] found that the ferrite phase in low-carbon steel was transformed into a harder martensite or bainite phase by the laser ablation and laser interference of LST. Li [159] constructed a bionic texture on the surface of 40Cr alloy steel. The bionic texture samples showed phase transformation and grain enhancement. After laser treatment, the microstructure of the bionic texture region was mainly composed of dense fine-grained martensite, compared with the microstructure of the matrix. As shown in Figure 37, the mechanism of surface enhancement by the laser bionic texture is the generation of the intensity phase, and the refinement of grains.

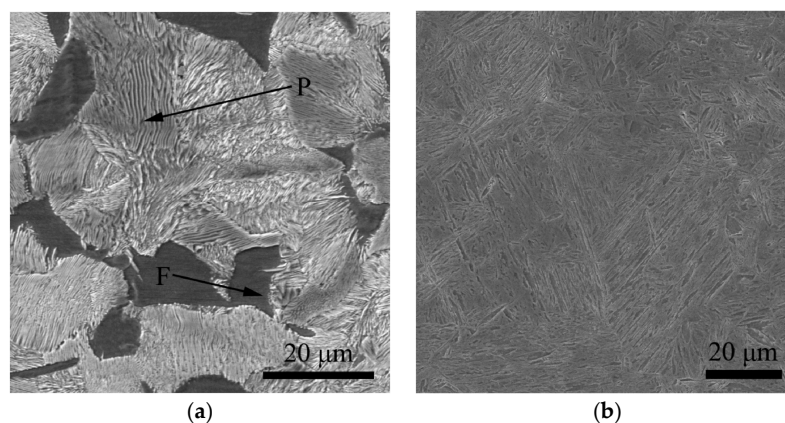


Figure 37. Microstructure before and after bionic texture construction [159]: (a) original microstructure; (b) microstructure of the bionic texture zone.

In the process of the wear test, the internal properties of the material will also change accordingly. By imitating soil animals, Chen [164] processed bionic units with a laser, and analyzed the microscopic morphology through wear experiments, as shown in Figure 38. It can be seen that the surface of the untreated sample had huge corrosion pits, and a large number of cracks. On the reticular and striped samples, serious defects usually appeared on the matrix near the unit, or at the junction of the matrix and unit. In addition, slight corrosion pits were also observed on the unit, but much smaller than the corrosion pits that occurred on the matrix.

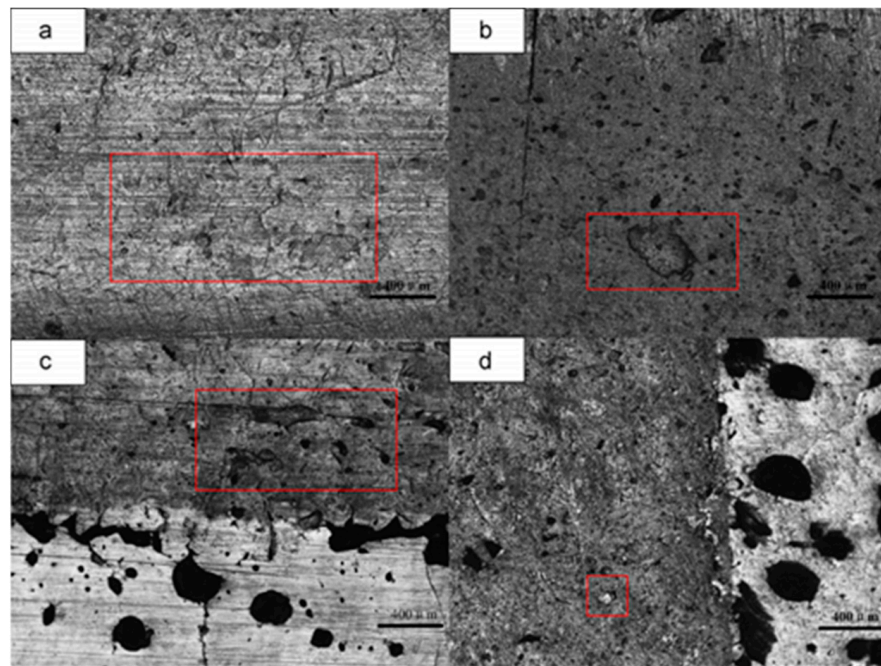


Figure 38. Contrast of wear mass loss between the original sample and bionic samples with diverse shapes, and the wear morphology of specimens [164]: (a) original sample; (b) the sample with punctate units; (c) striped units; (d) reticular units.

In order to improve the wear resistance of the material, Zheng [165] conducted the bionic coupling of the hardness gradient and surface texture. Through the hardness measurement along the depth of the cross-section sample, and correlation with the observation results of the metallographic microscope, the hexagonal texture sample quenched by laser heat treatment presented a gradual transformation of the melted layer, phase transformation zone, heat-affected zone, and unaffected matrix, from the surface to the interior, which mainly went through the phase-change process of needle-like martensite, granular martensite, and residual austenite, respectively. It was concluded that the theory of hardness decreasing from surface to interior was verified, and the bionic coupling had a lower friction coefficient, and a smaller friction fluctuation.

The high-strength phase can improve wear resistance, but it may also lead to the formation of surface cracks, and the generation of tensile residual stress. Therefore, specific analysis should be carried out on different parts of the components [166].

3.6.3. Wettability

Wettability has been a research focus in recent years, and there have been related research reports on different materials and textures, among which superhydrophobic properties are a key topic [167]. The essence of superhydrophobic properties is the change in the material surface structure and surface energy after processing, which affects the contact form between solid and liquid, resulting in a series of hydrophobic phenomena, with the characteristics of corrosion resistance and wear resistance.

The wettability of the texture surface is related to the shape, diameter, and depth of the texture. The texture can provide a thin layer of air, reduce the mutual attraction between the solid surface and the liquid, and make the surface show a hydrophobic effect, as shown in Figure 39 [168]. The main texture types for superhydrophobic surfaces are groove, grid, and columnar structures, in which the micro- and nano-composite structure, such as the lotus leaf, can show strong hydrophobicity. Bhushan [169] proposed an ideal superhydrophobic layered surface. For a droplet with a radius greater than, or equal to, 1 mm, the optimal design is a cylinder with a height H of 30 μm , diameter D of 15 μm , and pitch P of 130 μm , as shown in Figure 40 [170]. The micro-column array with small spacing, a small diameter, and a high height has a better hydrophobic effect [171].

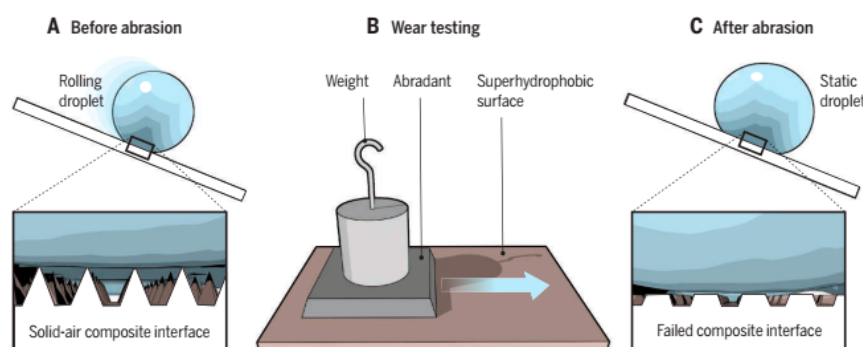


Figure 39. Wearing out a nonwetting surface. A superhydrophobic surface generally loses its liquid repellency after mechanical abrasion [168]: (A) a water droplet rolls on a superhydrophobic surface, where the liquid is suspended by a solid–air composite interface; (B) the setup for a linear abrasion test; (C) a droplet gets stuck on the same surface after abrasion, because of the failure of the composite interface.

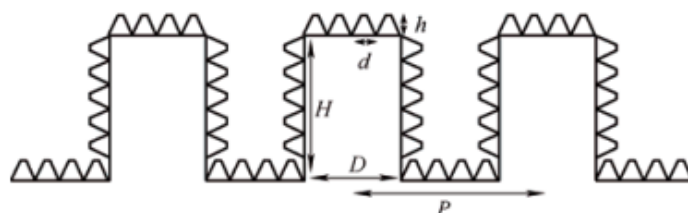


Figure 40. Ideal superhydrophobic layered surface [170].

The processing changes the chemical energy of the material surface which, in turn, changes its wettability. For example, ultrafast laser texturization will increase the chemical polarity of the material surface, so it appears hydrophilic. But over time, the non-polar bonds on the textured surface will increase, and the free energy will decrease, transforming into, and eventually maintaining, hydrophobicity. Divin-Mariotti [172] found that an aluminum surface, after femtosecond laser texturization, first showed hydrophilicity, and then changed to hydrophobicity after 3 days. Singh [173] found that the surface of 304 stainless steel after femtosecond laser action immediately showed superhydrophilic behavior and, after 50 days, showed highly hydrophobic behavior. Yan [174] studied the wettability changes of mixed micro–nano textured brass surfaces. By placing the samples in different media, such as air, NaHCO_3 solution, and NaCl solution, to explore the influence of the environment on the wettability transition rate, it was found that the textured brass sample could realize the transition from hydrophilic to hydrophobic after being soaked in isopropyl alcohol for 3 h.

4. Summary and Prospects

The significant advantages of water hydraulic transmission technology have meant that the research into water hydraulic axial piston pumps is commonly receiving attention

in the mechanical engineering and environmental engineering fields. The rapid development of special corrosion-resistant alloys, polymer materials, and engineering ceramics, and the progress in precision-machining technology, have effectively solved the key technical problems facing the research into water hydraulic axial piston pumps. With the development of water hydraulic axial piston pumps toward high speed and high pressure, more stringent requirements are being put forward for the tribological performance of the key friction pairs under extreme working conditions, such as high speed and a heavy load.

Inspired by the phenomenon of low friction and wear on the surface of natural organisms, the biomimetic surface texture design of the key friction pairs in water hydraulic axial piston pumps is considered to be an effective new approach to improving tribological properties. The structure and organization in nature can reduce friction contact, improve surface separation, and enhance mechanical properties, through the surface structure, self-secreted lubricating medium, and coupling effect of the structure and lubricating medium [116]. The common processing methods of the surface texture mainly comprise removing material technology (LST, mechanical machining, EDM, etc.), adding material technology (laser cladding, deposition technique, etc.), and deforming material technology (laser shock processing, etc.).

The tribological properties can be improved through the proper shape, equivalent diameter, depth, and arrangement of the surface texture. The lubrication antifriction mechanism of the surface texture is related to the lubrication state. The main lubrication mechanisms are the hydrodynamic effect and cavitation effect, secondary lubrication effect, and storage of wear debris, respectively, in fluid lubrication, boundary lubrication, and dry friction.

Many researchers have designed a variety of biomimetic structures, with the help of the surface appearance of organisms. The shapes of surface texture are mainly divided into four types: pits, grooves, convex bodies, and scales. Among them, pits and grooves have been studied the most frequently. There is a nonlinear relationship between the equivalent diameter of the surface texture, and the friction coefficient and the flow pressure. The equivalent diameter, greater than or less than the critical value of contact width, will have a significant effect on the lubricant film thickness. The research on the size of the micron level is mainly distributed between 10–1000 μm . The influence of the equivalent diameter of micro-texture on the friction performance is not obvious under low speed or high speed, but is obvious under medium speed. Under fluid lubrication, the depth of the surface texture plays a decisive role in the formation of the lubricant film. When it has a certain depth, a micro-vortex will be formed in the pit, affecting the hydrodynamic lubrication. Compared with the depth, using a depth-to-diameter ratio to describe the texture can better reflect its morphological characteristics. The effect of the depth-to-diameter ratio on the tribological properties is nonlinear. For different working conditions, there is an optimal ratio of texture depth and diameter, to obtain the best friction performance. The area ratio and the arrangement form of the surface texture have a great impact on friction and wear. For the area ratio, compared with other lubrication methods, dry friction requires a higher area ratio to obtain a smaller friction coefficient. Regarding the arrangement, staggered arrangements and circular arrangements are better than other arrangements.

There is no doubt that surface texture techniques offer promising prospects in the application of water hydraulic axial piston pumps, which have been shown to play a positive role in improving lubrication, reducing drag and friction, resisting wear, and decreasing vibration and noise. However, the research on surface texture still lacks a systematic approach. According to the research progress and application demands of surface texture, it is suggested that attention should be paid to the following aspects in the future:

- (1) Based on the study of pit texture, groove texture, and mixed texture, the lubrication antifriction properties of the complex shape texture and the cross-scale composite texture under complex type synergies need to be further studied.

- (2) Surfaces with different wettability can be obtained using surface coating techniques; this is helpful in further improving the tribological properties of the textured surface. The mechanism of coordinated regulating of lubrication and friction reduction under the coupling of the surface texture and coating/thin film system is still unclear, and needs to be further explored.
- (3) The actual friction and wear process of the textured surface is a dynamic process, in which the fluid, wall, and abrasive particles interact, and the friction coefficient, friction temperature, and wear change in a complex manner. A multi-scale and multi-field coupling method should be used to build a bridge from the micro-physical field to the macro-tribological properties, and the influence mechanism of the surface parameters, such as surface roughness, texture shape, and geometric parameters, and dynamic changes in the properties of the lubricating medium on the friction and wear properties of the sliding interface, should be studied.
- (4) The high processing cost and the low industrial manufacturing degree of surface texture (especially on the micro- and nano-level) are the main obstacles restricting the application of surface texture engineering. It is urgent to make breakthroughs in the technology of the processing, characterization, and evaluation of the micro- and nano-complex surface textures with a high efficiency, high quality, and low cost.

Author Contributions: Conceptualization, Y.L. and D.G.; methodology, Y.L.; validation, W.W. and Z.Z. (Zhepeng Zhang); formal analysis, H.X. and C.W.; investigation, Z.Z. (Zongyi Zhang) and T.G.; resources, Y.L.; data curation, W.W.; writing—original draft preparation, Y.L., C.W., W.W., Z.Z. (Zhepeng Zhang) and H.X.; writing—review and editing, D.G., Z.Z. (Zongyi Zhang) and T.G.; supervision, D.G.; project administration, Y.L.; funding acquisition, Y.L. and D.G. All authors have read and agreed to the published version of the manuscript.

Funding: This research was supported by the National Natural Science Foundation of China (Grant No. 52005428), the Hebei Natural Science Foundation (Grant No. E2020203107 and Grant No. E2021203099), Science and Technology Research Project of Colleges and Universities in Hebei Province (Grant No. ZD2020120), and the Open Fund Project of Shaanxi Provincial Key Laboratory of Hydraulic Technology (No. YYJS2022KF04).

Data Availability Statement: All data generated or analyzed during this study are included in this article.

Conflicts of Interest: The authors declare no conflict of interest.

Abbreviations

NCEL	Naval Civil Engineering Lab
PTFE	Polytetrafluoroethylene
PEEK	Polyether ether ketone
PI	Polyimide
PA	Polyamide
PPS	Polyphenylene sulfide
UHMWPE	Ultra high molecular weight polyethylene
OCP	Open circuit potential
CF	Carbon fiber
GF	Glass fiber
LST	Laser surface texturing
EDM	Electrical discharge machining
HA	Hyaluronic acid
DLC	Diamond-like carbon
CFD	Computational fluid dynamics
HV	Vickers hardness
UVAT	Ultrasonic vibration-assisted turning

References

1. Li, Z.Y.; He, X.F.; Yu, Z.Y.; Nie, S.L. Development opportunity and prospective for water hydraulic technology. *Fluid Power Transm. Control* **2003**, 13–19. (In Chinese)
2. Zhu, J.A.; Guo, P.H. Developing history of water hydraulic technology and its application in coal mine production. *Appl. Mech. Mater.* **2010**, *42*, 236–241. [[CrossRef](#)]
3. Yang, H.Y.; Zhou, H. New achievements in water hydraulics. *Chin. Hydraul. Pneum.* **2013**, *258*, 1–6. (In Chinese)
4. Liu, Y.S.; Li, Z.Y. *Hydraulic Components and Systems*, 4th ed.; China Machine Press: Beijing, China, 2019; p. 12. (In Chinese)
5. Lim, G.H.; Chua, P.S.K.; He, Y.B. Modern water hydraulics—the new energy-transmission technology in fluid power. *Appl. Energy* **2003**, *76*, 239–246. [[CrossRef](#)]
6. Nie, S.L.; Shi, X.Y.; Li, X.H.; Li, Z.Y. Water hydraulics and its applications in the agricultural machinery. *Trans. Chin. Soc. Agric. Mach.* **2006**, *37*, 193–198. (In Chinese)
7. Liu, L.Z.; Zhao, X.N.; Xie, E.Q. Analysis and Solution of the Influence of Mine Water on the Electric and Hydraulic Control System. *Adv. Mater. Res.* **2011**, 356–360, 1220–1224. [[CrossRef](#)]
8. Lu, Y.M.; Zhou, H. Water hydraulics in the food processing industry. *Chin. Hydraul. Pneum.* **2004**, 49–50. (In Chinese)
9. Wan, L. Push water hydraulic technology to wider application space. *Hydraul. Pneum. Seals* **2020**, *40*, 98–102. (In Chinese)
10. Guo, X.T.; Xing, T.; Ruan, J. Industrial application and new progress of hydraulic technology. *Chin. High Technol. Lett.* **2020**, *30*, 644–654. (In Chinese)
11. Zhou, H. Research on Seawater Hydraulic Pump and Its Basic Theory. Ph.D. Thesis, Huazhong University of Science and Technology, Wuhan, China, 1997. (In Chinese).
12. Wang, D.; Li, Z.Y.; Zhu, Y.Q. Lubrication and tribology in seawater hydraulic piston pump. *J. Mar. Sci. Appl.* **2003**, *2*, 35–40. [[CrossRef](#)]
13. Jiao, S.J.; Zhou, H.; Yang, H.Y.; Gong, G.F.; Chen, J.M.; Zhou, H.D. Tribological behavior of filled polyetheretherketone composites in sliding against stainless steel under water lubrication. *Tribology* **2003**, *23*, 385–389. (In Chinese)
14. Liang, X.X.; Yang, Z.Y. Experimental study on the influence of friction pair material hardness on the tribological behaviors of water lubricated thrust bearings. *Ind. Lubr. Tribol.* **2021**, *73*, 929–936. [[CrossRef](#)]
15. Zhai, X.; Ji, H.; Nie, S.L.; Yin, F.L.; Ma, Z.H. Effect of different Ni concentration on the corrosion and friction properties of WC-hNi/SiC pair lubricated with seawater. *Int. J. Refract. Met. Hard Mater.* **2022**, *102*, 105727. [[CrossRef](#)]
16. Yang, J.; Liu, Z.L.; Cheng, Q.C.; Liu, X.K.; Deng, T.Y. The effect of wear on the frictional vibration suppression of water-lubricated rubber slat with/without surface texture. *Wear* **2019**, 426–427, 1304–1317. [[CrossRef](#)]
17. Wang, Z.Q.; He, H.F.; Wu, S.F.; Xiang, J.B.; Ni, J. Effect of surface topography and wettability on friction properties of CFRPEEK. *Tribol. Int.* **2022**, *171*, 107573. [[CrossRef](#)]
18. Kong, X.; Sun, W.Y.; Wang, Q.C.; Chen, M.H.; Zhang, T.; Wang, F.H. Improving high-temperature wear resistance of NiCr matrix self-lubricating composites by controlling oxidation and surface texturing. *J. Mater. Sci. Technol.* **2022**, *131*, 253–263. [[CrossRef](#)]
19. Zhai, J. Investigation into the Key Problems of Axial Piston Pump for Seawater Desalination. Ph.D. Thesis, Zhejiang University, Hangzhou, China, 2012. (In Chinese).
20. Wu, D.F.; Li, B.; Chen, J.Y.; Liu, Y.S.; Li, Z.Y. Study on the tribological characteristics of slipper/swash plate pair of ultra-high seawater pump lubricated by water. *Chin. Hydraul. Pneum.* **2010**, *229*, 65–67. (In Chinese)
21. Bhushan, B.; Gray, S. *Investigation of Material Combinations under High Load and Speed in Synthetic Seawater*; ASLE: Reno, NV, USA, 1978.
22. Wen, H.X.; Sun, J.J.; Chen, W. Tribological study of the key friction pairs materials under seawater: Status quo and prospects. *Mater. Rep.* **2016**, *30*, 85–91+112. (In Chinese)
23. Liu, E.Y.; Zeng, Z.X.; Zhao, W.J. Corrosive wear and integrated anti-wear & anti-corrosion technology metallic materials in seawater. *Surf. Technol.* **2017**, *46*, 149–157. (In Chinese)
24. Li, W.Z.; Yan, N.; Deng, F.; Zhang, F.X. Research progress on friction and wear property of engineering plastics under water lubrication. *New Chem. Mater.* **2022**, *50*, 30–33+38. (In Chinese)
25. Zhang, J.; Su, X.L.; Shan, L.; Li, J.L.; Dong, M.P. Tribological behaviors of ceramic materials in seawater. *Lubr. Eng.* **2018**, *43*, 104–110+123. (In Chinese)
26. Cui, G.J.; Bi, Q.L.; Zhu, S.Y.; Yang, J.; Liu, W.M. Tribological behavior of Cu-6Sn-6Zn-3Pb under sea water, distilled water and dry-sliding conditions. *Tribol. Int.* **2012**, *55*, 126–134. [[CrossRef](#)]
27. Wu, H.R.; Bi, Q.L.; Yang, J.; Liu, W.M. Tribological performance of tin-based white metal ZChSnSb 8-8 under simulated sea water environment. *Tribology* **2011**, *31*, 271–277. (In Chinese)
28. Chen, J.; Li, Q.A.; Zhang, Q.; Fu, S.L.; Chen, X.Y. Effect of corrosion on wear resistance of several metals in seawater. *Trans. Mater. Heat Treat.* **2014**, *35*, 166–171. (In Chinese)
29. Zhang, Y.; Yin, X.Y.; Wang, J.Z.; Yan, F.Y. Influence of microstructure evolution on tribocorrosion of 304SS in artificial seawater. *Corros. Sci.* **2014**, *88*, 423–433. [[CrossRef](#)]
30. Dong, C.L.; Bai, X.Q.; Yan, X.P.; Yuan, C.Q. Research status and advances on tribological study of materials under ocean environment. *Tribology* **2013**, *33*, 311–320. (In Chinese)
31. Ding, H.Y.; Dai, Z.D. Corrosion wear characteristic of TC11 alloy in artificial seawater. *Tribology* **2008**, *28*, 139–144. (In Chinese)
32. Li, S.Z.; Dong, X.L. *Erosion Wear and Fretting Wear of Materials*; China Machine Press: Beijing, China, 1987; p. 280. (In Chinese)

33. Li, X.X.; Li, Y.X.; Wang, S.Q. Wear behavior and mechanism of tc4 alloy in different environmental media. *Chin. J. Rare Met.* **2015**, *39*, 793–798. (In Chinese)
34. Zhu, L.F. Study on the Tribocorrosion Behavior of 316L Stainless Steel and 2205 Duplex Steel in Seawater. Master's Thesis, Chengdu University of Technology, Chengdu, China, 2016. (In Chinese).
35. Zhang, Y.; Yin, X.Y.; Wang, J.Z.; Yan, F.Y. Influence of potentials on the tribocorrosion behavior of 304SS in artificial seawater. *RSC Adv.* **2014**, *4*, 55752–55759. [[CrossRef](#)]
36. Zhang, B.B.; Wang, J.Z.; Zhang, Y.; Han, G.F.; Yan, F.Y. Comparison of tribocorrosion behavior between 304 austenitic and 410 martensitic stainless steels in artificial seawater. *RSC Adv.* **2016**, *6*, 107933–107941. [[CrossRef](#)]
37. Chen, J.; Zhang, Q.; Li, Q.A.; Fu, S.L.; Wang, J.Z. Corrosion and tribocorrosion behaviors of AISI 316 stainless steel and Ti6Al4V alloys in artificial seawater. *Trans. Nonferrous Met. Soc. China* **2014**, *24*, 1022–1031. [[CrossRef](#)]
38. Chen, J.; Wang, J.Z.; Yan, F.Y.; Zhang, Q.; Li, Q.A. Effect of applied potential on the tribocorrosion behaviors of Monel K500 alloy in artificial seawater. *Tribol. Int.* **2015**, *81*, 1–8. [[CrossRef](#)]
39. Tao, Y.Q.; Liu, G.; Li, Y.S.; Zeng, Z.X. Corrosion wear properties of 2024 Al-alloy in artificial seawater. *J. Chin. Soc. Corros. Prot.* **2016**, *36*, 587–594. (In Chinese)
40. Wang, J.Z.; Yan, F.Y.; Xue, Q.J. Tribological behavior of PTFE sliding against steel in sea water. *Wear* **2009**, *267*, 1634–1641. [[CrossRef](#)]
41. Jia, J.H.; Chen, J.M.; Zhou, H.D.; Zhang, D.J.; Gu, Y.H. The tribological properties of carbon fiber reinforced PEEK composites under water lubrication. *Polym. Mater. Sci. Eng.* **2005**, *21*, 208–212. (In Chinese)
42. Jia, J.H.; Zhou, H.D.; Gao, S.Q.; Zhou, H.; Chen, J.M. The tribological behavior of carbon fiber reinforced polyimide composites under water lubrication. *Tribology* **2002**, *22*, 273–276. (In Chinese)
43. Wang, H.Q.; Cao, L.L.; Sun, S.Q. A study on friction and wear behavior of Nylon 1010 under water lubricating with A3 steel. *Tribology* **1997**, *17*, 152–159. (In Chinese)
44. Wei, X.C.; Su, Z.G.; Xu, B.M.; An, J.; Shen, Y.S.; Liu, S.Y. Friction and wear behaviours between GF/PA66 composite and Al₂O₃ ceramic. *Acta Mater. Compos. Sin.* **2012**, *29*, 47–52. (In Chinese)
45. Chen, Z.B.; Li, T.S.; Yang, Y.L.; Zhang, Y. Mechanical and tribological properties of PA66/PPS blends—(II) water lubrication. *Polym. Mater. Sci. Eng.* **2003**, *19*, 108–110+114. (In Chinese)
46. Xiong, D.S.; Gao, Z.; Jin, Z.M. Friction and wear properties of UHMWPE against ion implanted titanium alloy. *Surf. Coat. Technol.* **2007**, *201*, 6847–6850. [[CrossRef](#)]
47. Arash, G.; Klaus, F.; Andreas, N.; Braham, P. Tribological behavior of carbon-filled PPS composites in water lubricated contacts. *Wear* **2015**, *328–329*, 456–463.
48. Xiong, D.S. Friction and wear properties of UHMWPE composites reinforced with carbon fiber. *Mater. Lett.* **2005**, *59*, 175–179.
49. Zhang, J.G.; Cai, C.L. Friction and wear properties of carbon fiber reinforced PEEK composites under water lubrication. *Appl. Mech. Mater.* **2011**, *66–68*, 1051–1054. [[CrossRef](#)]
50. Yang, Q.P.; Huang, P. Friction and wear property of glass fiber filled polytetrafluoroethylene under sea water lubrication. *Mach. Tool Hydraul.* **2016**, *44*, 12–18. (In Chinese)
51. Xu, Y.K.; Guo, Y.X.; Li, G.T.; Zhang, L.G.; Zhao, F.Y.; Guo, X.P.; Dmitriev, A.I.; Zhang, G. Role of hydrolysable nanoparticles on tribological performance of PPS-steel sliding pair lubricated with sea water. *Tribol. Int.* **2018**, *127*, 147–156. [[CrossRef](#)]
52. Zhong, Y.J.; Xie, G.Y.; Sun, Z.S.; Sui, G.X. Study on the tribological properties of polyetheretherketone composites reinforced by ZrO₂ particles and short carbon fibers under water lubrication. *Chin. J. Mater. Res.* **2010**, *24*, 625–630. (In Chinese)
53. Xu, Y. A Study on Tribological Properties of Ceramic Class Composite Materials in Water. Master's Thesis, Nanjing University of Aeronautics and Astronautics, Nanjing, China, 2010. (In Chinese).
54. Tomizawa, H.; Fischer, T.E. Friction and wear of silicon nitride and silicon carbide in water: Hydrodynamic lubrication at low sliding speed obtained by tribochemical wear. *ASLE Trans.* **1987**, *30*, 41–46. [[CrossRef](#)]
55. Fischer, T.E.; Mullins, W.M. Chemical aspects of ceramic tribology. *J. Phys. Chem.* **1992**, *96*, 5690–5701. [[CrossRef](#)]
56. Matsuda, M.; Kato, K.; Hashimoto, A. Friction and wear properties of silicon carbide in water from different sources. *Tribol. Lett.* **2011**, *43*, 33–41. [[CrossRef](#)]
57. Gates, R.S.; Hsu, S.M. Tribochemistry between water and Si₃N₄ and SiC: Induction time analysis. *Tribol. Lett.* **2004**, *17*, 399–407. [[CrossRef](#)]
58. Liu, N.; Wang, J.Z.; Chen, B.B.; Yang, J.; Yan, F.Y. Tribological behavior of alumina ceramic under lubrication of seawater. *Lubr. Eng.* **2013**, *38*, 55–59. (In Chinese)
59. Wang, S.; Cheng, J.; Zhu, S.Y.; Qiao, Z.H.; Yang, J.; Liu, W.M. Frictional properties of Ti₃AlC₂ ceramic against different counterparts in deionized water and artificial seawater. *Ceram. Int.* **2016**, *42*, 4578–4585. [[CrossRef](#)]
60. Wang, S.; Cheng, J.; Zhu, S.Y.; Qiao, Z.H.; Yang, J. Low friction properties of Ti₃AlC₂/SiC tribo-pair in sea water environment. *Tribol. Int.* **2016**, *103*, 228–235. [[CrossRef](#)]
61. Wang, J.; Yan, F.; Xue, Q. Friction and wear behavior of ultra-high molecular weight polyethylene sliding against GCR15 steel and electroless Ni-P alloy coating under the lubrication of seawater. *Tribol. Lett.* **2009**, *35*, 85–95. [[CrossRef](#)]
62. Li, Y.; Qu, L.; Wang, F.H. The electrochemical corrosion behavior of TiN and (Ti,Al)N coatings in acid and salt solution. *Corros. Sci.* **2003**, *45*, 1367–1381. [[CrossRef](#)]
63. Liu, Z.Y.; Yin, W.; Tao, D.S.; Tian, Y. A glimpse of superb tribological designs in nature. *Biotribology* **2015**, *1*, 11–23. [[CrossRef](#)]

64. Wu, Z.; Bao, H.; Xing, Y.Q.; Liu, L. Tribological characteristics and advanced processing methods of textured surfaces: A review. *Int. J. Adv. Manuf. Technol.* **2021**, *114*, 1241–1277. [[CrossRef](#)]
65. Hamilton, D.B.; Walowitz, J.A.; Allen, C.M. A theory of lubrication by micro-irregularities. *J. Basic Eng.* **1966**, *88*, 177–185. [[CrossRef](#)]
66. Etsion, I.; Burstein, L. A model for mechanical seals with regular microsurface structure. *Tribol. Trans.* **1996**, *39*, 677–683. [[CrossRef](#)]
67. Etsion, I. State of the art in laser surface texturing. *J. Tribol.* **2005**, *127*, 248–253. [[CrossRef](#)]
68. Etsion, I.; Sher, E. Improving fuel efficiency with laser surface textured piston rings. *Tribol. Int.* **2009**, *42*, 542–547. [[CrossRef](#)]
69. Marian, M.; Shah, R.; Gashi, B.; Zhang, S.; Bhavnani, K.; Wartzack, S.; Rosenkranz, A. Exploring the lubrication mechanisms of synovial fluids for joint longevity—a perspective. *Colloids Surf. B Biointerfaces* **2021**, *206*, 111926. [[CrossRef](#)]
70. Bijani, D.; Deladi, E.L.; Akchurin, A.; De Rooij, M.B.; Schipper, D.J. The influence of surface texturing on the frictional behaviour of parallel sliding lubricated surfaces under conditions of mixed lubrication. *Lubricants* **2018**, *6*, 91. [[CrossRef](#)]
71. Gropper, D.; Wang, L.; Harvey, T.J. Hydrodynamic lubrication of textured surfaces: A review of modeling techniques and key findings. *Tribol. Int.* **2016**, *94*, 509–529. [[CrossRef](#)]
72. Yu, H.W.; Wang, X.L.; Zhou, F. Geometric shape effects of surface texture on the generation of hydrodynamic pressure between conformal contacting surfaces. *Tribol. Lett.* **2010**, *37*, 123–130. [[CrossRef](#)]
73. Etsion, I.; Kligerman, Y.; Halperin, G. Analytical and experimental investigation of laser-textured mechanical seal faces. *Tribol. Trans.* **1999**, *42*, 511–516. [[CrossRef](#)]
74. Yu, H.W.; Deng, H.S.; Huang, W.; Wang, X.L. Effects of micro-dimple arrangements on tribological performance of sliding surfaces. *J. China Univ. Min. Technol.* **2011**, *40*, 943–948. (In Chinese)
75. Liao, W.L. The influence of contact mode of friction pair on the hydrodynamic lubrication performance of textured surface. *J. Chengdu Technol. Univ.* **2020**, *23*, 1–9. (In Chinese)
76. Borghi, A.; Gualtieri, E.; Marchetto, D.; Moretti, L.; Valeri, S. Tribological effects of surface texturing on nitriding steel for high-performance engine applications. *Wear* **2008**, *265*, 1046–1051. [[CrossRef](#)]
77. Varenberg, M.; Halperin, G.; Etsion, I. Different aspects of the role of wear debris in fretting wear. *Wear* **2002**, *252*, 902–910. [[CrossRef](#)]
78. Volchok, A.; Halperin, G.; Etsion, I. The effect of surface regular microtopography on fretting fatigue life. *Wear* **2002**, *253*, 509–515. [[CrossRef](#)]
79. Li, T.T.; Sun, Y.N.; Zhang, L.; Wang, G.J. Research progress on effect of surface texturing on tribological properties. *Mater. Mech. Eng.* **2020**, *44*, 44–48. (In Chinese)
80. Ito, H.; Kaneda, K.; Yuhta, T.; Nishimura, I.; Yasuda, K.; Matsuno, T. Reduction of polyethylene wear by concave dimples on the frictional surface in artificial hip joints. *J. Arthroplast.* **2000**, *15*, 332–338. [[CrossRef](#)] [[PubMed](#)]
81. Gachot, C.; Hsu, A.; Rosenkranz, S.M.; Costa, H.L. A critical assessment of surface texturing for friction and wear improvement. *Wear* **2017**, *372–373*, 21–41. [[CrossRef](#)]
82. Mao, B.; Siddaiah, A.; Liao, Y.L.; Menezes, P.L. Laser surface texturing and related techniques for enhancing tribological performance of engineering materials: A review. *J. Manuf. Process.* **2020**, *53*, 153–173. [[CrossRef](#)]
83. Wang, X.J.; Liu, J.Y.; Wang, Y.; Fu, Y.N. Fabrication of friction-reducing texture surface by selective laser melting of ink-printed (SLM-IP) copper (Cu) nanoparticles (NPs). *Appl. Surf. Sci.* **2017**, *396*, 659–664. [[CrossRef](#)]
84. Wang, H.; Kalchev, Y.; Wang, H.C.; Yan, K.; Gurevich, E.L.; Ostendorf, A. Surface modification of NiTi alloy by ultrashort pulsed laser shock peening. *Surf. Coat. Technol.* **2020**, *394*, 125899. [[CrossRef](#)]
85. Babu, P.V.; Ismail, S.; Ben, B.S. Experimental and numerical studies of positive texture effect on friction reduction of sliding contact under mixed lubrication. *Proc. Inst. Mech. Eng. Part J J. Eng. Tribol.* **2021**, *235*, 360–375. [[CrossRef](#)]
86. Xie, J.; Xie, H.F.; Luo, M.J.; Tan, T.W.; Li, P. Dry electro-contact discharge mutual-wear truing of micro diamond wheel V-tip for precision micro-grinding. *Int. J. Mach. Tools Manuf.* **2012**, *60*, 44–51. [[CrossRef](#)]
87. Jain, A.; Kumari, N.; Jagadevan, S.; Bajpai, V. Surface properties and bacterial behavior of micro conical dimple textured Ti6Al4V surface through micro-milling. *Surf. Interfaces* **2020**, *21*, 100714. [[CrossRef](#)]
88. Iacono, F.; Pirani, C.; Generali, L.; Sassatelli, P.; Nucci, C.; Gandolfi, M.G.; Prati, C. Wear analysis and cyclic fatigue resistance of electro discharge machined NiTi rotary instruments. *G. Ital. Di Endod.* **2016**, *30*, 64–68. [[CrossRef](#)]
89. Natarajan, Y.; Murugesan, P.K.; Mohan, M.; Khan, S.A.L.A. Abrasive water jet machining process: A state of art of review. *J. Manuf. Process.* **2020**, *49*, 271–322. [[CrossRef](#)]
90. Hernández-Castellano, P.M.; Benítez-Vega, H.A.N.; Díaz-Padilla, N.; Ortega-García, F.; Socorro-Perdomo, P.; Marrero-Alemán, M.D.; Salguero, J. Design and manufacture of structured surfaces by electroforming. *Procedia Manuf.* **2017**, *13*, 402–409. [[CrossRef](#)]
91. Lauwers, B. Surface integrity in hybrid machining processes. *Procedia Eng.* **2011**, *19*, 241–251. [[CrossRef](#)]
92. Wang, Z.Q.; Fu, Q.; Wood, R.J.K.; Wu, J.; Wang, S.C. Influence of bionic non-smooth surface texture on tribological characteristics of carbon-fiber-reinforced polyetheretherketone under seawater lubrication. *Tribol. Int.* **2020**, *144*, 106100. [[CrossRef](#)]
93. Liang, Y.N.; Gao, D.R.; Chen, B.; Zhao, J.H. Friction and wear study on friction pairs with a biomimetic non-smooth surface of 316L relative to CF/PEEK under a seawater lubricated condition. *Chin. J. Mech. Eng.* **2019**, *32*, 66. [[CrossRef](#)]
94. Vilhena, L.; Sedlaček, M.; Podgornik, B.; Rek, Z.; Žun, I. CFD modeling of the effect of different surface texturing geometries on the frictional behavior. *Lubricants* **2018**, *6*, 15. [[CrossRef](#)]

95. Zhang, H.F.; Zhang, P.; Sui, Q.; Zhao, K.; Zhou, H.; Ren, L.Q. Influence of multiple bionic unit coupling on sliding wear of laser-processed gray cast iron. *J. Mater. Eng. Perform.* **2017**, *26*, 1614–1625. [[CrossRef](#)]
96. Wang, H.H.; Lin, N.M.; Yuan, S.; Liu, Z.Q.; Yu, Y.; Zeng, Q.F.; Li, D.Y.; Fan, J.F.; Wu, Y.C. Numerical simulation on hydrodynamic lubrication performance of bionic multi-scale composite textures inspired by surface patterns of subcrenata and clam shells. *Tribol. Int.* **2023**, *181*, 108335. [[CrossRef](#)]
97. Wu, Z.M.; Yuan, C.Q.; Guo, Z.W.; Huang, Q.R. Effect of the groove parameters on the lubricating performance of the water-lubricated bearing under low speed. *Wear* **2023**, *522*, 204708. [[CrossRef](#)]
98. Zhang, H.; Hua, M.; Dong, G.Z.; Zhang, D.Y.; Chen, W.J.; Dong, G.N. Optimization of texture shape based on Genetic Algorithm under unidirectional sliding. *Tribol. Int.* **2017**, *115*, 222–232. [[CrossRef](#)]
99. Zhang, N.; Yang, F.Z.; Jiang, F.L.; Zhang, Y.; Liu, G.H. Investigation of tribological performance of micro-groove textured cemented carbide surfaces. *Surf. Eng.* **2020**, *36*, 1190–1199. [[CrossRef](#)]
100. Guo, Q.G.; Zheng, L.; Zhong, Y.H.; Wang, S.K.; Ren, L.Q. Numerical simulation of hydrodynamic lubrication performance for continuous groove-textured surface. *Tribol. Int.* **2022**, *167*, 107411. [[CrossRef](#)]
101. Dong, G.N.; Zhang, H.; Chin, K.S.; Hua, M. Improvement of tribological behaviors by optimizing concave texture shape under reciprocating sliding motion. *J. Tribol.* **2017**, *139*, 011701.
102. Luo, Y.H. Recent progress in exploring drag reduction mechanism of real sharkskin surface: A review. *J. Mech. Med. Biol.* **2015**, *15*, 1530002. [[CrossRef](#)]
103. Brian, D.; Bharat, B. Shark-skin surfaces for fluid-drag reduction in turbulent flow: A review. *Philos. Trans. R. Soc. A* **2010**, *368*, 5737.
104. Huang, Q.P.; Shi, X.L.; Ma, J. Tribological behavior of surface bionic rhombic-textured M50 steel containing SnAgCu and MXene-Nb₂C under dry sliding Conditions. *J. Mater. Eng. Perform.* **2021**, *30*, 9390–9402. [[CrossRef](#)]
105. Hatakeyama, H.; Hatakeyama, T. Interaction between water and hydrophilic polymers. *Thermochim. Acta* **1998**, *308*, 3–22. [[CrossRef](#)]
106. Zhao, H.X.; Sun, Q.Q.; Deng, X.; Cui, J.X. Earthworm-inspired rough polymer coatings with self-replenishing lubrication for adaptive friction-reduction and antifouling surfaces. *Adv. Mater.* **2018**, *30*, 1802141. [[CrossRef](#)]
107. Wu, Y.H.; Dong, C.L.; Bai, X.Q.; Yuan, C.Q.; Zhang, X.J. A novel green and low friction composite reinforced by lignum vitae chips. *Polym. Test.* **2022**, *115*, 107768. [[CrossRef](#)]
108. Hakala, T.J.; Saikko, V.; Arola, S.; Ahlroos, T.; Helle, A.; Kuosmanen, P.; Holmberg, K.; Linder, M.B.; Laaksonen, P. Structural characterization and tribological evaluation of quince seed mucilage. *Tribol. Int.* **2014**, *77*, 24–31. [[CrossRef](#)]
109. Xu, X.Y.; Wu, J.N.; Yang, Y.Q.; Zhu, R.G.; Yan, S.Z. Operculum of a water snail is a hydrodynamic lubrication sheet. *J. Bionic Eng.* **2018**, *15*, 471–480. [[CrossRef](#)]
110. Furukawa, K.; Ochiai, M.; Hashimoto, H.; Kotani, S. Bearing characteristic of journal bearing applied biomimetics. *Tribol. Int.* **2020**, *150*, 106345. [[CrossRef](#)]
111. Guo, Z.W.; Xin, X.; Yuan, C.Q.; Bai, X.Q. Study on influence of micro convex textures on tribological performances of UHMWPE material under the water-lubricated conditions. *Wear* **2019**, *426–427*, 1327–1335. [[CrossRef](#)]
112. Guo, Z.W.; Yuan, C.Q.; Liu, A.X.; Jiang, S. Study on tribological properties of novel biomimetic material for water-lubricated stern tube bearing. *Wear* **2017**, *376–377*, 911–919. [[CrossRef](#)]
113. Burris, D.L.; Moore, A.C. Cartilage and joint lubrication: New insights into the role of hydrodynamics. *Biotribology* **2017**, *12*, 8–14. [[CrossRef](#)]
114. Chen, C.; Xia, Y.Q.; Cao, Z.F. Brasenia Schreberi mucilage as a green lubricant additive exhibiting good tribological properties for steel/steel and steel/aluminium friction pairs. *Mater. Res. Express* **2022**, *9*, 025503. [[CrossRef](#)]
115. Liu, P.X.; Liu, Y.H.; Yang, Y.; Chen, Z.; Li, J.J.; Luo, J.B. Mechanism of biological liquid super lubricity of Brasenia schreberi mucilage. *Langmuir ACS J. Surf. Colloids* **2014**, *30*, 3811–3816. [[CrossRef](#)] [[PubMed](#)]
116. Li, X.F.; Guo, Z.W.; Huang, Q.R.; Yuan, C.Q. Application of bionic tribology in water-lubricated bearing: A review. *J. Bionic Eng.* **2022**, *19*, 902–934. [[CrossRef](#)]
117. Xu, Y.F.; Peng, Y.; Dearn, K.D.; You, T.; Geng, J.; Hu, X.G. Fabrication and tribological characterization of laser textured boron cast iron surfaces. *Surf. Coat. Technol.* **2017**, *313*, 391–401. [[CrossRef](#)]
118. Marian, M.; Zambrano, D.F.; Rothhammer, B.; Waltenberger, V.; Boidi, G.; Krapf, A.; Merle, B.; Stampfl, J.; Rosenkranz, A.; Gachot, C.; et al. Combining multi-scale surface texturing and DLC coatings for improved tribological performance of 3D printed polymers. *Surf. Coat. Technol.* **2023**, *466*, 129682. [[CrossRef](#)]
119. Sun, Q.C.; Hu, T.C.; Fan, H.Z.; Zhang, Y.S.; Hu, L.T. Dry sliding wear behavior of TC11 alloy at 500 °C: Influence of laser surface texturing. *Tribol. Int.* **2015**, *92*, 136–145. [[CrossRef](#)]
120. Yu, H.W.; Huang, W.; Wang, X.L. Dimple patterns design for different circumstances. *Lubr. Sci.* **2013**, *25*, 67–78. [[CrossRef](#)]
121. Costa, H.L.; Hutchings, I.M. Hydrodynamic lubrication of textured steel surfaces under reciprocating sliding conditions. *Tribol. Int.* **2007**, *40*, 1227–1238. [[CrossRef](#)]
122. Wang, X.L.; Adachi, K.S.; Otsuka, K.; Kato, K.J. Preliminary investigation of the effect of dimple size on friction in line contacts. *Tribol. Int.* **2009**, *42*, 1118–1123. [[CrossRef](#)]
123. Yin, B.F.; Li, X.D.; Fu, Y.H.; Yun, W. Effect of laser textured dimples on the lubrication performance of cylinder liner in diesel engine. *Lubr. Sci.* **2012**, *24*, 293–312. [[CrossRef](#)]

124. Kovalchenko, A.; Ajayi, O.; Erdemir, A.; Fenske, G.; Etsion, I. The effect of laser surface texturing on transitions in lubrication regimes during unidirectional sliding contact. *Tribol. Int.* **2005**, *38*, 219–225. [[CrossRef](#)]
125. Chouquet, C.; Gavillet, J.; Ducros, C.; Sanchette, F. Effect of DLC surface texturing on friction and wear during lubricated sliding. *Mater. Chem. Phys.* **2010**, *123*, 367–371. [[CrossRef](#)]
126. Pettersson, U.; Jacobson, S. Friction and wear properties of micro textured DLC coated surfaces in boundary lubricated sliding. *Tribol. Lett.* **2004**, *17*, 553–559. [[CrossRef](#)]
127. Tang, H.S.; Ren, Y.; Kumar, A. Optimization tool based on multi-objective adaptive surrogate modeling for surface texture design of slipper bearing in axial piston pump. *Alex. Eng. J.* **2021**, *60*, 4483–4503. [[CrossRef](#)]
128. Shen, X.H.; Tao, G.C. Tribological behaviors of two micro textured surfaces generated by vibrating milling under boundary lubricated sliding. *Int. J. Adv. Manuf. Technol.* **2015**, *79*, 1995–2002. [[CrossRef](#)]
129. Mourier, L.; Mazuyer, D.; Ninove, F.P.; Lubrecht, A.A. Lubrication mechanisms with laser-surface-textured surfaces in elastohydrodynamic regime. *Proc. Inst. Mech. Eng. Part J J. Eng. Tribol.* **2010**, *224*, 697–711. [[CrossRef](#)]
130. Hou, Q.M.; Yang, X.F.; Cheng, J.; Wang, S.R.; Duan, D.R.; Xiao, J.P.; Li, W.Y. Optimization of performance parameters and mechanism of bionic texture on friction surface. *Coatings* **2020**, *10*, 171. [[CrossRef](#)]
131. Mourier, L.; Mazuyer, D.; Lubrecht, A.A.; Donnetet, C. Transient increase of film thickness in micro-textured EHL contacts. *Tribol. Int.* **2006**, *39*, 1745–1756. [[CrossRef](#)]
132. Kaneta, M.; Kanada, T.; Nishikawa, H. Optical interferometric observations of the effects of a moving dent on point contact EHL. *Tribol. Ser.* **1997**, *32*, 69–79.
133. Sahlin, F.; Glavatskih, S.; Almqvist, T.; Larsson, R. Two-dimensional CFD-analysis of micro-patterned surfaces in hydrodynamic lubrication. *J. Tribol.* **2005**, *127*, 96–102. [[CrossRef](#)]
134. Han, J.; Fang, L.; Sun, J.P.; Ge, S.R. Hydrodynamic lubrication of microdimple textured surface using three-dimensional CFD. *Tribol. Trans.* **2010**, *53*, 860–870. [[CrossRef](#)]
135. He, X.; Zhong, L.; Wang, G.R.; Liao, Y.; Liu, Q.Y. Tribological behavior of femtosecond laser textured surfaces of 20CrNiMo/beryllium bronze tribo-pairs. *Ind. Lubr. Tribol.* **2015**, *67*, 630–638. [[CrossRef](#)]
136. Kim, B.; Chae, Y.H.; Choi, H.S. Effects of surface texturing on the frictional behavior of cast iron surfaces. *Tribol. Int.* **2014**, *70*, 128–135. [[CrossRef](#)]
137. Hu, D.; Guo, Z.W.; Xie, X.; Yuan, C.Q. Effect of spherical-convex surface texture on tribological performance of water-lubricated bearing. *Tribol. Int.* **2019**, *134*, 341–351. [[CrossRef](#)]
138. Li, K.M.; Jing, D.L.; Hu, J.; Ding, X.H.; Yao, Z.Q. Numerical investigation of the tribological performance of micro-dimple textured surfaces under hydrodynamic lubrication. *Beilstein J. Nanotechnol.* **2017**, *8*, 2324–2338. [[CrossRef](#)] [[PubMed](#)]
139. Zhang, Y.L.; Zhang, X.G.; Wu, T.H.; Xie, Y.B. Effects of surface texturing on the tribological behavior of piston rings under lubricated conditions. *Ind. Lubr. Tribol.* **2016**, *68*, 158–169. [[CrossRef](#)]
140. Shimizu, J.; Nakayama, T.; Watanabe, K.; Yamamoto, T.; Onuki, T.; Ojima, H.; Zhou, L. Friction characteristics of mechanically microtextured metal surface in dry sliding. *Tribol. Int.* **2020**, *149*, 105634. [[CrossRef](#)]
141. Hu, T.C.; Hu, L.T.; Ding, Q. Effective solution for the tribological problems of Ti-6Al-4V: Combination of laser surface texturing and solid lubricant film. *Surf. Coat. Technol.* **2012**, *206*, 5060–5066. [[CrossRef](#)]
142. Meng, R.; Deng, J.X.; Liu, Y.Y.; Duan, R.; Zhang, G.L. Improving tribological performance of cemented carbides by combining laser surface texturing and W-S-C solid lubricant coating. *Int. J. Refract. Met. Hard Mater.* **2018**, *72*, 163–171. [[CrossRef](#)]
143. Li, Y.J.; Pang, X.J.; Sun, L.M.; Niu, Y.X.; Zhang, Y.Z. Effects of laser surface texturing on friction and wear properties of 45 steel. *Surf. Technol.* **2018**, *47*, 147–154. (In Chinese)
144. Wei, P.L. Research on Friction Characteristics of Surface Point Contact Lubrication and Kite-Shaped Texture Lubrication. Master's Thesis, Xi'an University of Technology, Xi'an, China, 2020. (In Chinese)
145. Wakuda, M.; Yamauchi, Y.; Kanzaki, S.; Yasuda, Y. Effect of surface texturing on friction reduction between ceramic and steel materials under lubricated sliding contact. *Wear* **2003**, *254*, 356–363. [[CrossRef](#)]
146. Yang, X.P.; Fu, Y.H.; Ji, J.H.; Chen, T.Y.; Pan, C.Y. Study on tribological properties of surface concave convex micro-texture on the mold steel. *Ind. Lubr. Tribol.* **2020**, *72*, 1167–1171. [[CrossRef](#)]
147. Xu, Y.F.; Zheng, Q.; Abuflaha, R.; Olson, D.; Furlong, O.; You, T.; Zhang, Q.Q.; Hu, X.G.; Tysoe, W.T. Influence of dimple shape on tribofilm formation and tribological properties of textured surfaces under full and starved lubrication. *Tribol. Int.* **2019**, *136*, 267–275. [[CrossRef](#)]
148. Zhong, Y.H.; Zheng, L.; Gao, Y.H.; Liu, Z.N. Numerical simulation and experimental investigation of tribological performance on bionic hexagonal textured surface. *Tribol. Int.* **2019**, *129*, 151–161. [[CrossRef](#)]
149. Wang, G.R.; Liao, D.S.; Zhong, L.; Liao, W.L.; Wei, G. Effect of groove-like surface texture on friction performance of plunger seal pair. *Surf. Technol.* **2019**, *48*, 165–173. (In Chinese)
150. Wang, J.F.; Qian, W.; Wang, D. Effect of surface texture arrangements on lubrication characteristics. *Lubr. Eng.* **2015**, *40*, 86–90. (In Chinese)
151. Yi, M.H.; Chen, G.D.; Gao, D.C.; Su, H.; Wang, L. Effects of micro texture on the dynamic characteristics of journal bearing. *J. Northwestern Polytech. Univ.* **2015**, *33*, 658–664. (In Chinese)
152. Wang, H.T.; Zhu, H. Effect of cylindrical micro-pit's distribution form on tribology properties of textured surface. *Tribology* **2014**, *34*, 414–419. (In Chinese)

153. Zhang, H.; Liu, Y.; Hua, M.; Zhang, D.Y.; Qin, L.G.; Dong, G.N. An optimization research on the coverage of micro-textures arranged on bearing sliders. *Tribol. Int.* **2018**, *128*, 231–239. [[CrossRef](#)]
154. Schneider, J.; Braun, D.; Greiner, C. Laser textured surfaces for mixed lubrication: Influence of aspect ratio, textured area and dimple arrangement. *Lubricants* **2017**, *5*, 32. [[CrossRef](#)]
155. Yue, H.Z.; Deng, J.X.; Ge, D.L.; Li, X.M.; Zhang, Y. Effect of surface texturing on tribological performance of sliding guideway under boundary lubrication. *J. Manuf. Process.* **2019**, *47*, 172–182. [[CrossRef](#)]
156. Antoszewski, B.; Kurp, P. Effect of surface texture on the sliding pair lubrication efficiency. *Lubricants* **2022**, *10*, 80. [[CrossRef](#)]
157. Guo, Y.B.; Caslaru, R. Fabrication and characterization of micro dent arrays produced by laser shock peening on titanium Ti-6Al-4V surfaces. *J. Mater. Process. Technol.* **2011**, *211*, 729–736. [[CrossRef](#)]
158. Garcia-Giron, A.; Romano, J.M.; Liang, Y.; Dashtbozorg, B.; Dong, H.; Penchev, P.; Dimov, S.S. Combined surface hardening and laser patterning approach for functionalising stainless steel surfaces. *Appl. Surf. Sci.* **2018**, *439*, 516–524. [[CrossRef](#)]
159. Li, H.; Zhou, H.; Zhang, D.P.; Zhang, P.; Zhou, T. Influence of varying distribution distance and angle on fatigue wear resistance of 40Cr alloy steel with laser bionic texture. *Mater. Chem. Phys.* **2022**, *277*, 125515. [[CrossRef](#)]
160. Hussein, H.T.; Kadhim, A.; Al-Amieri, A.A.; Kadhum, A.A.H.; Mohamad, A.B. Enhancement of the wear resistance and microhardness of aluminum alloy by Nd:YAG laser treatment. *Sci. World J.* **2014**, *2014*, 842062. [[CrossRef](#)]
161. Amini, S.; Hosseinabadi, H.N.; Sajjadi, S.A. Experimental study on effect of micro textured surfaces generated by ultrasonic vibration assisted face turning on friction and wear performance. *Appl. Surf. Sci.* **2016**, *390*, 633–648. [[CrossRef](#)]
162. Ji, R.; Zhao, Q.; Zhao, L.; Liu, Y.; Jin, H.; Wang, L.; Wu, L.; Xu, Z. Study on high wear resistance surface texture of electrical discharge machining based on a new water-in-oil working fluid. *Tribol. Int.* **2023**, *180*, 108218. [[CrossRef](#)]
163. Syed, B.; Shariff, S.M.; Padmanabham, G.; Lenka, S.; Bhattacharya, B.; Kundu, S. Influence of laser surface hardened layer on mechanical properties of re-engineered low carbon steel sheet. *Mater. Sci. Eng. A-Struct. Mater. Prop. Microstruct. Process.* **2017**, *685*, 168–177. [[CrossRef](#)]
164. Chen, Z.K.; Lu, S.C.; Song, X.B.; Zhang, H.; Yang, W.S.; Zhou, H. Effects of bionic units on the fatigue wear of gray cast iron surface with different shapes and distributions. *Opt. Laser Technol.* **2015**, *66*, 166–174. [[CrossRef](#)]
165. Zheng, L.; Wu, J.; Zhang, S.; Sun, S.; Zhang, Z.; Liang, S.; Liu, Z.; Ren, L. Bionic coupling of hardness gradient to surface texture for improved anti-wear properties. *J. Bionic Eng.* **2016**, *13*, 406–415. [[CrossRef](#)]
166. Ezhilmaran, V.; Vijayaraghavan, L.; Vasa, N.J. Investigation of Nd³⁺:YAG laser aided surface texturing to improve tribological characteristics of piston ring. *J. Laser Micro Nanoeng.* **2017**, *12*, 195–202.
167. Khaskhoussi, A.; Risitano, G.; Calabrese, L.; D'Andrea, D. Investigation of the wettability properties of different textured lead/lead-free bronze coatings. *Lubricants* **2022**, *10*, 82. [[CrossRef](#)]
168. Tian, X.L.; Verho, T.; Ras, R.H.A. Moving superhydrophobic surfaces toward real-world applications. *Science* **2016**, *352*, 142–143. [[CrossRef](#)]
169. Bhushan, B.; Jung, Y.C.; Koch, K. Micro-, nano- and hierarchical structures for superhydrophobicity, self-cleaning and low adhesion. *Philos. Trans. R. Soc. A-Math. Phys. Eng. Sci.* **2009**, *367*, 1631–1672. [[CrossRef](#)]
170. Bhushan, B.; Jung, Y.C. Wetting, adhesion and friction of superhydrophobic and hydrophilic leaves and fabricated micro/nanopatterned surfaces. *J. Phys. Condens. Matter* **2008**, *20*, 225010. [[CrossRef](#)]
171. Wu, S.Z.; Li, D.Y.; Huang, J.H.; Xiang, L.; Lu, J.W.; Wang, Y.; Li, J.Q.; Li, C.Z. Fabrication of bionic hydrophobic micropillar arrays by femtosecond lasers for droplet manipulation. *Chin. Sci. Bull.* **2022**, *67*, 1958–1965. (In Chinese) [[CrossRef](#)]
172. Divin-Mariotti, S.; Amieux, P.; Pascale-Hamri, A.; Auger, V.; Kermouche, G.; Valiorgue, F.; Valette, S. Effects of micro-knurling and femtosecond laser micro texturing on aluminum long-term surface wettability. *Appl. Surf. Sci.* **2019**, *479*, 344–350. [[CrossRef](#)]
173. Singh, A.K.; Kumar, B.S.; Jha, P.; Mahanti, A.; Singh, K.; Kain, V.; Sinha, S. Surface micro-structuring of type 304 stainless steel by femtosecond pulsed laser: Effect on surface wettability and corrosion resistance. *Appl. Phys. A* **2018**, *124*, 846. [[CrossRef](#)]
174. Yan, H.P.; Rashid, M.R.B.A.; Khew, S.Y.; Li, F.P.; Hong, M.H. Wettability transition of laser textured brass surfaces inside different mediums. *Appl. Surf. Sci.* **2018**, *427*, 369–375. [[CrossRef](#)]

Disclaimer/Publisher's Note: The statements, opinions and data contained in all publications are solely those of the individual author(s) and contributor(s) and not of MDPI and/or the editor(s). MDPI and/or the editor(s) disclaim responsibility for any injury to people or property resulting from any ideas, methods, instructions or products referred to in the content.